DOTTORATO DI RICERCA IN

SCIENZE CLINICHE

CICLO XXXIV

COORDINATORE Prof. Lorenzo Cosmi

Role of both pre-treatment CT in the upper respiratory airways pathology of cystic fibrosis patients and MRI Diffusion (DwI) - perfusion (DCE-PwI) in diagnosis, predicting pre-treatment response and treatment monitoring in head and neck neoplasms

Settore Scientifico Disciplinare MED/36

Dottorando

Dott. Pietragalla Michele

Tutore

Dott. Cosimo Nardi

Coordinatore

Prof. Lorenzo Cosmi

Prof. COSMI LORENZO
Matr. 999314

Anni 2018/2021

ROLE OF BOTH PRE-TREATMENT CT IN THE UPPER RESPIRATORY AIRWAYS PATHOLOGY OF CYSTIC FIBROSIS PATIENTS AND MRI DIFFUSION (DWI) - PERFUSION (DCE-PWI) IN DIAGNOSIS, PREDICTING PRE-TREATMENT RESPONSE AND TREATMENT MONITORING IN HEAD AND NECK NEOPLASMS

Table of contents

Part one

Role of pre-treatment CT in the upper respiratory airways pathology of cystic fibrosis

Synthesis

The two main purposes of this observational retrospective study were to evaluate the sinonasal anatomical differences between adult patients with cystic fibrosis (CF) and patients without CF and, secondly, to compare the surgically relevant anatomy on computed tomography (CT) scan of patients with CF versus patients without CF undergoing endoscopic sinus surgery (ESS), in terms of risk of developing postoperative complications. The results obtained was recently published (2021) in the international scientific journal *"Laryngoscope"* with the title *"The Risks of Complications During Endoscopic Sinus Surgery in Cystic Fibrosis Patients: An Anatomical and Endoscopic Study"*. The contents of the article are summarized below.

CF is an autosomal recessive disorder characterized by a defect in the cystic fibrosis transmembrane conductance regulator (CFTR) gene on chromosome 7. CFTR mutations profoundly alter sinonasal development in patients with CF. Historically regarded as a pediatric disease, thanks to the development of new pharmacological treatments, now CF is an adult condition, with a current median survival of 37 to 42 years. Chronic rhinosinusitis (CRS) with or without nasal polyposis affects nearly one-half of all patients with CF, as a result of their propensity to produce thick mucus and of the impairment of mucociliary clearance. Moreover, direct CT notably reveals radiological signs of inflammation in almost 100% of patients with CF. Therefore, an increasing proportion of adult patients with CF is being referred to ESS in order to relieve the symptoms of CRS. ESS is widely accepted as the standard of care after the failure of adequate medical treatment with some authors supporting upfront "extended" ESS (e.g., modified medial maxillectomy/MEMM, Draf III procedures) in these patients. However, ESS is associated with a potential risk of serious complications that occur in about 0.5% to 1% of patients without CF, and it was shown that preoperative CT imaging is able to identify anatomical variants at risk for their occurrence. How these anatomical variants influence the operative risk is unclear.

The first part of the present study was purely dedicated to analysing the anatomical differences between 103 patients with CF and 100 patients without CF with CRS evaluated in two referral centers (AOU Careggi and AOU Meyer, both in Florence, Italy) from January 2012 to January 2020. The preoperative unenhanced CT scans of these patients were reviewed according to the CLOSE checklist in order to assess the presence of critical anatomical variants in patients with CF and patients without CF.

The second part of the study consisted of the comparison of patients with CF versus patients without CF who underwent primary or revision ESS for CRS with and without polyposis. Postoperative complications (within 30 days) were classified according to a three-tiered system proposed by Siedek et al.: grade I (minor complications such as periorbital ecchymosis), grade II (major events, e.g., cerebrospinal fluid leak), and grade III (serious/life-threatening complications such as injury to the optic nerve or internal carotid artery).

The frontal sinus pneumatization was defined with a four-tiered scale (hyperplasia; normal size; hypoplasia; and aplasia) on coronal planes (Fig. 1). The sphenoid sinus pneumatization was classified as pre-sellar, sellar, and post-sellar on sagittal planes (Fig. 2). The width, depth, and height of maxillary sinuses were measured according to two different models (Fig.3). The mean maxillary sinus volume was estimated with a mathematical formula (=height × width × depth × 0.52). The following paranasal anatomical variants were also evaluated: position of the lateral nasal wall (LNW) with respect to the orbital wall (lamina papiracea) (Fig.4), depth of the olfactory fossa by measuring the height of the lateral lamella (Keros scheme), the distance from the anterior nasal spine to the nasofrontal break and anterior sphenoid wall

(Fig.6), position of the anterior ethmoidal canal (Fig.7), and presence of bony sclerosis (chronic osteitis), uncinate process demineralization, concha bullosa, paradoxical turbinate, and Onodi and infraorbital ethmoid cells.

The degree of inflammation in adult patients without CF with CRS was determined using the Lund-Mackay system. In these patients, 0 was assigned to sinuses with no mucosal thickening, 2 was assigned to opacified sinuses, and 1 was assigned to everything in between. Frontal, ethmoid, maxillary, and sphenoid sinuses and the ostiomeatal complex on each side were scored with a maximum of 24. A modification of this system that accounts for aplastic sinuses was used in the CF group: this was done by multiplying the patient's total score by 24 and dividing by the possible total for that patient (24–2 × number of missing structures).

As reported in Table I, in patients with CF the mean maxillary sinus dimensions were significantly smaller than those of patients without CF; the frontal and sphenoid sinuses were also significantly less pneumatized in the former group. Compared to patients without CF, uncinate process demineralization, maxillary infundibulum enlargement, and chronic osteitis were more commonly found in patients with CF; on the contrary, concha bullosa was rarely identified and infraorbital ethmoid cells were absent in all patients with CF. More than half of the CF population showed a Keros type I olfactory fossa, while, in the non-FC group, a Keros type II was the most represented finding (86%). The anterior ethmoidal artery bone canal was more frequently absent in patients without CF and this difference was statistically significant ($P < .001$). The mean distances from the anterior nasal spine to nasofrontal break and from the anterior nasal spine to the anterior wall of the sphenoid sinus were similar in the two groups. No difference was observed in terms of the frequency of Onodi cells, middle paradoxical turbinates, and LNW medialization between the two populations. The mean modified Lund-Mackay score of patients with CF was 12.42 and it was significantly higher than Lund-Mackay mean score calculated for patients without CF (5.88, $P < .001$).

A total of 47 patients with CF and 100 patients without CF underwent primary or revision ESS. The distribution of surgically relevant anatomical variants according to the CLOSE checklist in these groups is given in Table II. Patients without CF showed a significantly deeper olfactory fossa and a more frequent supraorbital pneumatization compared to patients with CF ($P < .001$ and $P = .031$, respectively). Whereas this latter group underwent more often aggressive ESS procedures such as MEMM ($P = .001$), no difference in terms of postoperative adverse events was found ($P = .620$) and in both groups, there was no postoperative grade III complication (Table III).

In conclusion, despite a profoundly altered sinonasal anatomy, patients with CF did not show an increased risk of surgical complications after ESS in our study. More aggressive endoscopic procedures in order to adequately open the affected sinuses may be safely performed in these patients where the reduced pneumatization might also be regarded as a protective factor against inadvertent injuries.

Tables

Paranasal sinus	Landmark	Patients with CF (103)		Patients without CF (100)		P	K
		Right	Left	Right	Left		
Maxillary	Width x depth x height (mm) [Jasim]	29,7(4,6) x 19(3,7) x 33,3(4,8)	29,4(4,2) x 19,2(3,5) x 34(4,8)	36,7(3,7) x 25,6(3,6) x 36,1(4,3)	36,6(3,9) x 26,3(3,9) x 37,4(5)	< 0.001	0.92
	Volume (ml) [Jasim]	9.7 (2.3)	10 (1.7)	17.6 (3.5)	18.7 (4.1)	< 0.001	0.91
	Width x depth x height (mm) [Sahlstrand-Johnson]	28(4,4) x 20,4(3,8) x 28,3(5)	27,4(4,2) x 20,6(3,6) x 29,1(5)	35,3(3,5) x 26,8(3,5) x 32,7(4,3)	35,5(3,5) x 27,5(3,8) x 33,7(4,7)	< 0.001	0.92
	Volume (ml) [Sahlstrand-Johnson]	8.4 (3.1)	8.2 (2.2)	16.1 (1.9)	17.1 (5.7)	< 0.001	0.90
	Hypoplasia	72 (69.9%)		0		< 0.001	0.91
	Lateral nasal wall medialization	68 (66%)		67 (67%)		0.344	0.87
	Infundibulum enlargement	85 (82.5%)		18 (18%)		< 0.001	0.89
	Mean infundibulum width (mm)	9 (4.1)		3.2 (2.4)		< 0.001	0.87
Sphenoid	Pre-sellar	55 (53.4%)		0		<0.001	0.95
	Sellar	39 (37.9%)		16 (16%)			
	Post-sellar	9 (8.7%)		84 (84%)			
Frontal	Aplasia	28 (27.2%)		0		<0.001	0.97
	Hypoplasia	33 (32%)		12 (12%)			
	Normal	40 (38.8%)		76 (76%)			
	Hyperplasia	2 (2%)		12 (12%)			
Ethmoid	Olfactory fossa Keros Type I	58 (56.3%)		12 (12%)		<0.01	0.93
	Olfactory fossa Keros Type II	45 (43.7%)		86 (86%)			
	Olfactory fossa Keros Type III	0		2 (2%)			

	Uncinate process demineralization	71 (68.9%)	20 (20%)	< 0.001	0.89
	Distance from the nasal spine to nasofrontal beak (mm)	48.3 (3.8)	49.1 (3.8)	0.162	0.95
	Distance from the nasal spine to the anterior wall of the sphenoid sinus (mm)	57.1 (3.6)	56.1 (3.5)	0.047	0.96
	Anterior ethmoidal artery bone canal (right/left)	88 (85.4%) / 86 (83.5%)	50 (50%) / 54 (54%)	<0.001/<0.001	0.92
	Infraorbital cell	0	6 (6%)	0.049	0.89
	Spheno-ethmoidal cell	10 (9.7%)	18 (18%)	0.867	0.88
Others	**Presence of Chronic osteitis**	87 (84.5%)	22 (22%)	<0.001	0.79
	Concha bullosa	3 (2.9%)	22 (22%)	<0.001	0.89
	Paradoxical middle turbinate	2 (1.9%)	6 (6%)	0.137	0.95

Table 1. An anatomical and radiological description of the paranasal sinuses in the two groups. Continuous variables are expressed as mean and SD in brackets while absolute count and percentage are given for categorical variables. p: p-value; K: Cohen's kappa coefficient for CT interobserver reliability.

CLOSE		Patients with CF (n= 47)	Patients without CF (n=100)	P-values
Cribriform plate: Deep of the olfactory fossa (Keros classification)	**Type I**	30 (63.8%)	14 (14%)	<0.001
	Type II	17 (36.2%)	83 (83%)	
	Type III	0	3 (1.6%)	
Lamina papiracea: Orbital prolapse/infraorbital ethmoidal Cells	**Present**	0	9 (9%)	0.058
	Absent	47 (100%)	91 (91%)	
Onodi Cell	**Present**	6 (10.3%)	4 (14%)	0.839
	Absent	41 (87.2%)	86 (86%)	
Sphenoid Sinus: Degree of pneumatization	**Pre-sellar**	24 (51.1%)	1 (1%)	<0.001
	Sellar	20 (42.5%)	21 (21%)	
	Post-sellar	3 (6.4%)	78 (78%)	
Sphenoid Sinus: Dehiscence of the carotid artery canal	**Present**	1 (2.1%)	9 (9%)	0.123
	Absent	46 (97.9%)	91 (91%)	
Ethmoidal artery (anterior): supraorbital pneumatization	**Present**	6 (12.8%)	29 (29%)	0.031
	Absent	41 (87.2%)	71 (71%)	

Table 2. Distribution of the critical anatomic structures, according to the CLOSE checklist, identified at the preoperative CT scan in the two groups who underwent ESS. Variables are expressed as absolute count and percentage in brackets.

Features	Patiens with CF (n=47)	Patients without CF (n=100)	P-value
Mean age at ESS	37.3 (8.2)	39.8 (10.4)	0.149
Male sex	29 (61.7%)	63 (63%)	0.879
Preoperative LMS (median)	16	15	0.72
Presence of nasal polyps	39 (83%)	73 (73%)	0.185
Type of ESS performed **Standard FESS** **MEMM** **Draf III Procedure**	 32 (68%) 15 (32%) 0 (0%)	 89 (89%) 8 (8%) 3 (3%)	0.001
Length of hospital stay (mean, days)	3.6 (1.4)	1.4 (0.8)	<0.001
Perioperative Complications **Overall** **Grade I** **Grade II** **Grade III**	 3 (6.4%) 3 (6.4%) 0 (0) 0 (0)	 8 (8%) 6 (6%) 2 (2%) 0 (0)	0.620

Table 2. A general description of the population who underwent endoscopic sinus surgery (ESS).
Continuous variables are expressed as mean and SD in brackets while absolute count and percentage are given for categorical variables. LMS = Lund–Mackay score; MEMM = modified endoscopic medial maxillectomy.

Figures

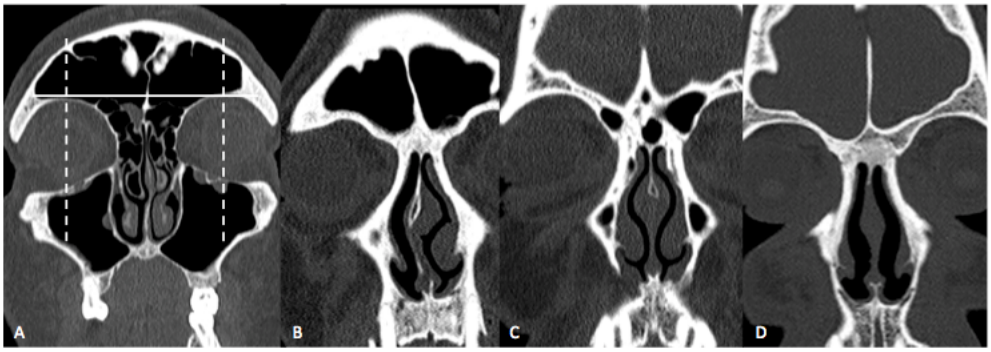

Fig. 1. According to the Guerram classification, the extension of the frontal sinus pneumatization was classified in four degrees: (A) Hyperplasia: pneumatization extending laterally to a line passing through the midorbit: dashed line); (B) Normal size: pneumatization extended above a line that joins both supraorbital rims (supraorbital line: continuous line); (C) Hypoplasia: pneumatization extended below the supraorbital line; (D) Aplasia: pneumatization absent.

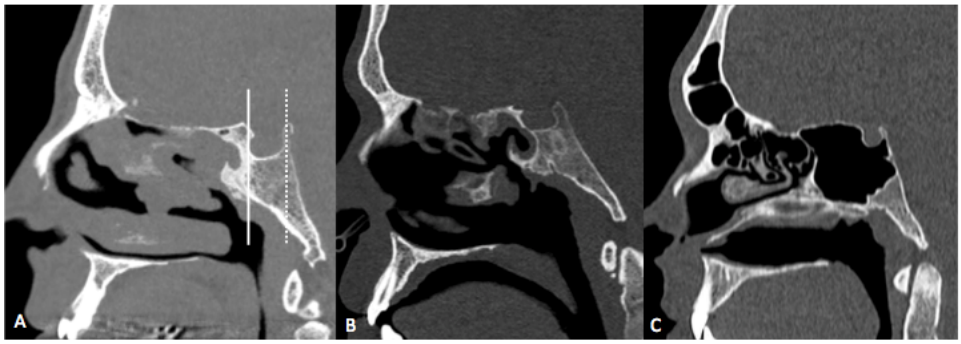

Fig. 2. The extension of the sphenoid sinus pneumatization was defined by drawing two vertical lines through the tuberculum sellae (continuous line) and the dorsum sellae (dotted line), respectively. (A) Pre-sellar: sphenoid pneumatization not reaching the tuberculum sellae. (B) Sellar: sphenoid pneumatization extending beyond the tuberculum sellae but not reaching the dorsum sellae. (C) Post-sellar: sphenoid pneumatization extending beyond the dorsum sellae.

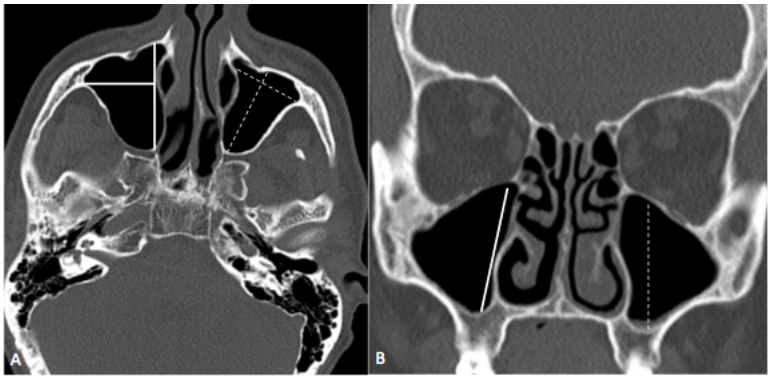

Fig. 3. Maxillary sinus dimension measurements: according to Jasim et al., the width was measured by drawing a perpendicular line from the medial sinus wall to the most distant lateral sinus wall (A, continuous medio-lateral line), the depth by drawing a line from the most anterior to the most posterior point of the medial sinus wall (A, continuous antero-posterior line), and the height by drawing a line from the lowest point of the sinus floor to the highest point of the sinus roof at the opening of the maxillary infundibulum (B, continuous cranio-caudal line). Following Sahlstrand-Johnson et al., the maximum width (A, dashed medio-lateral line), depth (A, dashed antero-posterior line), and height (B, dashed cranio-caudal line) of the maxillary sinus were also measured.

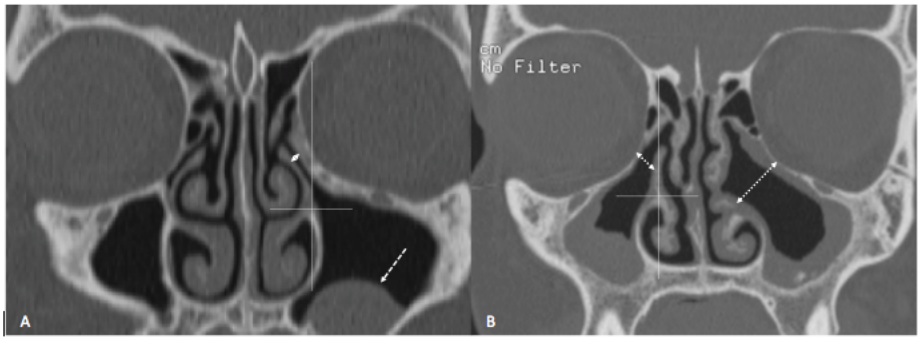

Fig. 4. (A) A 47-year male patient without cystic fibrosis (CF) with CRS. The width of the maxillary infundibulum was measured on the coronal plane at its largest dimension (double arrows). The position of the lateral nasal wall (LNW) was assessed by drawing two perpendicular lines through the uncinate process and the LNW junction (continuous perpendicular lines). LNW was lateral to the lamina papiracea in this case and a mucous retention pseudocyst is seen in the left maxillary sinus (dashed arrow). (B) CT of a 35-year male patient with CF revealed medialization of the LNW (continuous perpendicular lines), and enlargement of both maxillary sinus infundibula (dotted double arrowed lines).

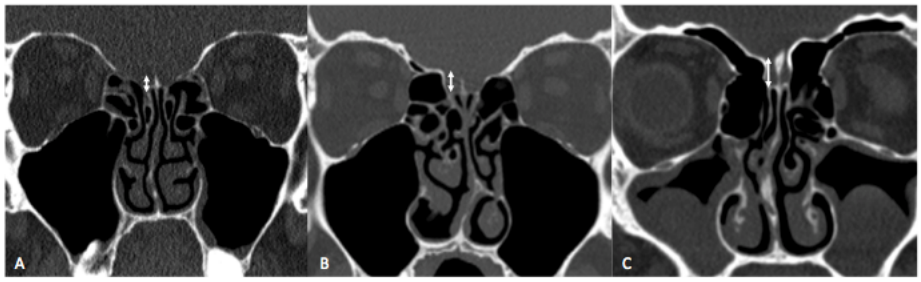

Fig. 5. According to Keros classification, the deep of the olfactory fossa was classified in three grades by measure the height of the ethmoid lateral lamella (double arrowed lines). A) grade I from 1 to 3 mm; B) grade II from 4 to 8 mm; C) grade III from 8 to 16 mm.

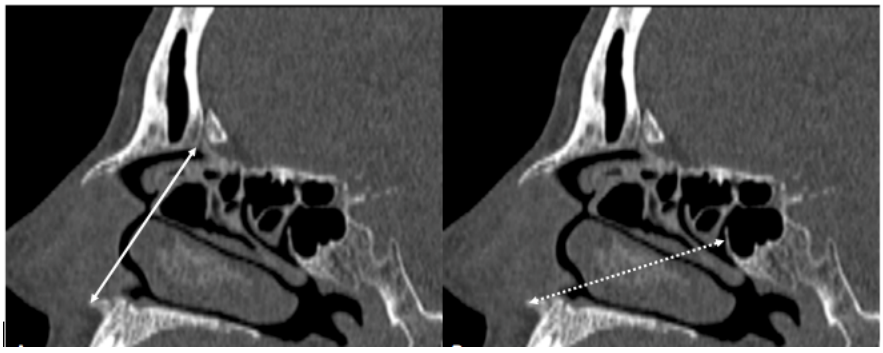

Fig. 6. The distances from the anterior nasal spine to nasofrontal break (A, double arrowed line), and from the anterior nasal spine to the anterior wall of the sphenoid sinus (B, double dotted arrowed line) were obtained as defined by Alimoglu et al.

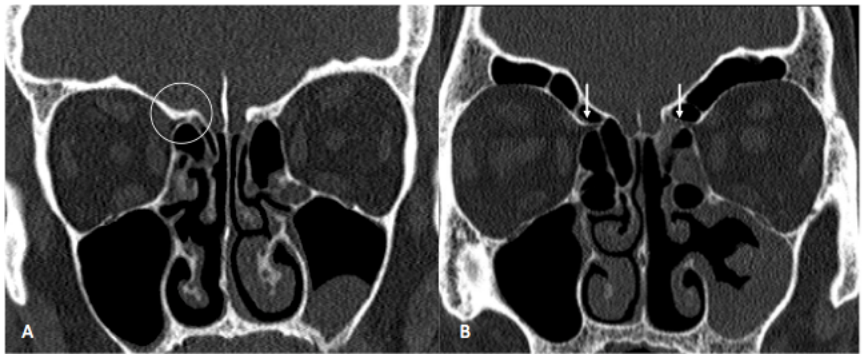

Fig 7. Anterior ethmoidal artery osseous canal was defined directly in contact with the skull base (A, white circle) or separated from ethmoid roof in case of air cells interposition (B, white arrows).

Part two

Role of MRI Diffusion (DWI) and perfusion (DCE-PWI) in predicting pre-treatment response and treatment monitoring in head and neck cancer

Abstract

Introduction: Head and neck squamous cell carcinomas (HNSCC) most frequently originate from oral cavity, oropharynx, and larynx. Over the past decade radio- and chemotherapy (CRT) have become more popular because of the better organ preservation; however, there is still a 35–65% recurrence rate. The successful pre-treatment identification of patients with resistant HNSCC would allow the CRT regimes to be modified or changed to a salvage surgery. The evaluation of post-treatment HNSCC patients is also crucial, but despite the availability of advanced imaging techniques, the interpretation of post-treatment follow-up imaging studies is complicated by altered anatomy, and post-actinic edema and fibrosis. A functional approach with Diffusion Weighted Imaging (DWI) and dynamic contrast-enhanced Perfusion Weighted Imaging (DCE-PWI) on Magnetic Resonance Imaging (MRI) can better characterize tumour behaviour.

Objective: The first aim of this retrospective study was to evaluate the usefulness of MRI with functional DWI and DCE-PWI sequences in distinguishing between post-CRT expected changes and neoplastic persistence/recurrence in patients with primary naso-oropharyngeal carcinoma. Secondary endpoint was to predict tumoral response to CRT on pre-treatment MRI images.

Material and methods: Morphologic, DWI and DCE-PWI MRI of 37 patients (19 males, 18 females; mean age 59 years, range 36–81 years) affected by nasopharyngeal and oropharyngeal carcinoma were assessed. Apparent diffusion coefficient (ADC) values were calculated by drawing three regions of interest with an average area of 0.30-0.40 cm^2 each on three contiguous axial sections. Area under curve (AUC) and K(trans) values were generated from DCE-PWI images by drawing a region of interest that included at least 50% of the largest lesion section. Vessels, calcifications, and necrotic/hemorrhagic or cystic areas within solid components were excluded.

The following features were considered on both MRI performed for tumour staging and 3-4 months follow-up: signal intensity of primitive tumour and residual tissue after CRT on T2-weighted and DWI_{b800} images; maximum size of primitive tumour and submucosal enhancement thickness of the residual tissue after CRT on post-contrast T1-weighted images; median ADC values, K(trans) and AUC values of primitive tumour (ADC_{pre}, AUC_{pre}, and $K(trans)_{pre}$) and residual tissue after CRT (ADC_{post}, AUC_{post}, and $K(trans)_{post}$) on DWI and DCE-PWI MRI sequences, respectively; ratio between AUC and K(trans) values of post-CRT residual tissue and primitive tumour, standardized with respect to AUC and K(trans) values of the ipsilateral trapezius muscle, respectively ($AUC_{post/pre/muscle}$ and $K(trans)_{post/pre/muscle}$).

The diagnosis of tumour response to CRT or tumoral persistence/recurrences was defined on follow-up with clinical examination and cross-sectional imaging including PET-CT for at least 12 months after MRI. Post-treatment biopsy was performed only in patients with positive PET-CT during follow-up. Clinical examination and MRI images were used to validate negative results as true negatives in patients with negative PET-CT during follow-up and without post-treatment biopsy or in patients with negative post-treatment biopsy results. Histology from endoscopic biopsy was performed in case of 12 patients with positive PET-CT (5 tumoral persistence/recurrences and 7 negative biopsy), whereas imaging alone was available in 25 patients with negative PET-CT during follow-up (all post-CRT changes).

Results: Submucosal enhancement thickness of post-treatment residual tissue was markedly different between post-CRT changes (mean 3.3 mm, range 0-10.3 mm) and tumour persistence/recurrence (mean 22.7 mm, range 7.2-45.4 mm). Median ADC_{post} was significantly greater in post-CRT alterations ($1.56 \pm 0.23 \times 10^{-3}$ mm^2/s) than in tumour recurrence ($1.06 \pm 0.27 \times 10^{-3}$ mm^2/s). In detecting patients with post-CRT changes, ADC_{post} values > 1.33×10^{-3} mm^2/s had sensitivity 84.6% and specificity 100% (P= 0.002), a percentage increase > 65.0% among median ADC_{post} values compared to median ADC_{pre} values ($ADC_{post\text{-}pre\%}$) showed sensitivity 76.9% and specificity 75.0% (P= 0.005), and value > 0.72×10^{-3} mm^2/s in the difference between median ADC_{post} and ADC_{pre} values ($ADC_{post\text{-}pre}$) had sensitivity 42.9% and specificity 100% (P= 0.052).

The signal intensity evaluation on $DWIb_{800}$ images of the residual tissue after CRT showed sensitivity 93.7%, specificity 80.0%, positive predictive value 96.8%, negative predictive value 66.6%, and diagnostic accuracy 91.8%. DWI_{b800} images showed a hypointense signal intensity in 30 out of 32 patients with post-CRT changes, and in only 1 out of 5 patients with tumour recurrence.

Mean $AUC_{post/pre/muscle}$ and mean $K(trans)_{post/pre/muscle}$ values were similar in patients with post-CRT alterations (1.10 ± 0.58, range 0.37-2.70; 1.08 ± 0.91, range 0.37-4.01, respectively) compared to patients with tumour recurrence (1.09 ± 0.11, range 0.92-1.18; 1.03 ± 0.12, range 0.87-1.14).

No significant difference was found in DWI and DCE-PWI values measured on pre-treatment MRI between patients with post-CRT changes and tumour persistence/recurrence at follow-up.

Conclusion: DWI and DCE-PWI functional sequences, in association with morphological criteria, were useful in the distinction between post-CRT treatment changes and tumoral persistence/recurrence in patients affected by primary nasopharyngeal and oropharyngeal carcinoma. ADC_{post} values > 1.33×10^{-3} mm^2/s and $ADC_{post\text{-}pre}$ values > 0.72×10^{-3} mm^2/s identified patients with post-CRT changes with excellent specificity (100%). For $AUC_{post/pre/muscle}$ and $K(trans)_{post/pre/muscle}$, values < 0.85 were suggestive for post-CRT fibrosis, values ≈1 (range 0.85-1.2) were found in tumoral persistence/recurrence, and higher values indicated inflammatory edema.

No significant difference was found in DWI and DCE-PWI values measured on pre-treatment MRI between patients with post-CRT changes and tumour persistence/recurrence. Further studies are needed to evaluate the usefulness of pre-treatment DWI and DCE-PWI MRI in predicting tumour response to CRT.

Introduction

Head and neck cancers represent the sixth most common cancer worldwide. More than 90% of head and neck cancers are squamous cell carcinomas (HNSCC) arising from the mucosal surfaces of the oral cavity, oropharynx, and larynx [1]. Crucial risk factors allied with head and neck cancer include tobacco, alcohol consumption, and human papilloma virus (HPV) [2] and Epstein-Barr virus (for nasopharyngeal cancer) infections. The chronic exposure of the upper aero digestive tract to these carcinogenic factors can result in dysplastic or premalignant lesions in the oropharyngeal mucosa ultimately resulting in head and neck cancer [3].

Over the past decade radio- and chemotherapy (CRT) have become more popular because of the better organ preservation [4]. In patients with advanced stage HNSCC, CRT is the standard organ-sparing treatment; however, there is still a 50% (35–65%) recurrence rate [5]. The risk of tumour recurrence is lower for early stage HNSCC (up to 25%) [6]. Almost 90% of HNSCC recurrences following CRT develop within 2 years [7]. Approximately 15% of patients with primary HNSCC develop second primary head and neck cancer [8].

The successful pre-treatment identification of patients with resistant HNSCC would allow the CRT regimes to be modified or changed to a salvage surgery [9].

The evaluation of post-treatment HNSCC patients is also crucial; early detection of recurrent HNSCC prompts curative salvage treatment and may allow preservation of organ function [6]. Despite the availability of advanced imaging techniques, the interpretation of post-treatment follow-up imaging studies is complicated by altered anatomy, and post-actinic edema and fibrosis. Most patients have a suboptimal clinical examination on account of pain and trismus, further compounding an already complex scenario. Post-treatment changes result in fibrosis, edema, and at times necrosis within the soft tissues, making it difficult for the radiologist to detect recurrent neoplastic disease within this distorted anatomy [10]. A biopsy with negative findings does not exclude HNSCC recurrence, and multiple biopsies may increase overall morbidity [6]. Therefore, in addition to clinical and histological parameters, other sophisticated biomarkers are needed to stratify patients for optimal therapy [11].

Morphologic Magnetic Resonance Imaging (MRI) is accurate in assessing deep tumour invasion and morphological tumour features, but it isn't able to identify early locoregional recurrence, to detect nodal metastasis in normal-sized lymph nodes, to predict tumour response to treatment or to monitor post-treatment changes [12, 13]. Imaging signs have been described in the literature that can help the radiologist differentiate post-treatment changes from recurrent tumour disease. These signs, however, have limitations and most patients have to undergo histopathology [3].

Metabolic imaging with 18F fluorodeoxyglucose PET-CT (FDG-PET) has evolved as a tool for the post-treatment evaluation of HNSCC but is generally delayed for at least 12 weeks due to the potential for false-positive resulting from early post-treatment inflammatory changes [14].

Nowadays, a multiparametric investigation was proposed with a combination of diffusion weighted (DWI) and dynamic contrast-enhanced imaging (DCE-PWI) MRI [15, 16]. According to the literature, this functional approach can better characterize tumour biology and behaviour [17]. DWI can by means of apparent diffusion coefficient (ADC) quantitatively characterize different tissue compartments [18, 19] and microstructures (i.e., cellularity, necrosis, stroma, hemorrhage) [11, 20]. DWI is based on the measurement of Brownian random motion of water molecules within a tissue voxel during the application of a pair of equal and opposite gradients (b value). The greater the movement of the water molecules during the signal acquisition, the greater the proton dephasing and the greater the T2* voxel signal fall. In inflammatory tissue diffusion is increased, and water protons undergo a dephasing due to their movement along the gradient itself, with loss of signal. Conversely, within neoplastic tissue water molecules have restricted diffusion and undergo an equal and opposite phase change during the application of both gradients without significant dephasing, with

consequent signal maintenance. ADC is a number expressed in mm^2/s derived by arithmetical combination of low and high b value images and it's an excellent parameter to define the presence of true restricted diffusion [21]. Thus, ADC can theoretically distinguish between inflammation and neoplastic tissue.

DCE-PWI MRI can assess microvascular parameters of tissue perfusion [22]. Given that induction of angiogenesis is a hallmark of cancer and the high level of evidence that tumour hypoxia is associated with a poor prognosis in head and neck cancer, it may be possible to use DCE-MRI to create a biological and prognostic profile to select patients most likely to benefit from chemotherapy and to improving or modified patient's treatment [8]. Moreover, with the increasing use of antiangiogenic agents, the assessment of the reduction of tumour vasculature is necessary to evaluate the response to therapy as well as to reduce the size of the tumour [23]. DCE-PWI is performed by obtaining rapid sequential T1-weighted MRI images through an area of interest before, during, and after the intravenous administration of a gadolinium-based contrast agent. This allows for temporal acquisition of T1 intensity at each point in space within the area of interest. By incorporating baseline T1 mapping before contrast administration, DCE-PWI allows transformation of a time-signal intensity curve (I/t) into a time concentration curve. These curves qualitatively reflect the passage of contrast agent media between vascular and extravascular extracellular space (EES) and the rate of uptake and clearance of contrast, which can be used to derive microvascular properties and semiquantitative parameters like area under the I/t (AUC). Using a bicompartmental pharmacokinetic model (Tofts model), it's possible to calculate quantitative parameters useful in clinical practice: K(trans), the volume transfer constant from the vascular space to the EES; K(ep), the rate constant from the EES to the vascular space; V(e), the volume of the EES per unit volume of tissue and V(p), total blood plasma volume [12, 24]. Recent literature highlights the K(trans) parameter. K(trans) reflects the combined effect of plasma blood flow, permeability and capillary surface area. Thus, K(trans) may be sensitive to angiogenic modifications of a neoplastic tissue [25].

In summary, MRI is a multiparametric technique with great potentials. Functional MRI can provide fundamental information in order to predict tumour response and distinguish between post-treatment changes and neoplastic recurrence/relapse and itis ideally suited to serial scanning, including repeat scanning early in the course of treatment, reducing the use of ionizing radiation [24, 26, 27]. The first aim of this study was to evaluate the usefulness of MRI with functional DWI and DCE-PWI sequences in distinguishing between post-CRT expected changes and neoplastic persistence/recurrence in patients with primary naso-oropharyngeal carcinoma. Secondary endpoint was to predict tumoral response to CRT on pre-treatment MRI images.

Materials and Methods

Inclusion criteria- From January 2016 to June 2021 all patients with histological diagnosis of carcinoma of the nasopharynx and oropharynx who underwent head and neck MRI in the radiology department of Careggi Hospital (Florence, Italy) were retrospectively included. The number of retrieved patients was 104. All procedures performed in studies involving human participants were in accordance with the ethical standards of the institutional and/or national research committee and with the 1964 Helsinki Declaration and its later amendments or comparable ethical standards. Informed consent was obtained from all individual participants included in the study.

Patients who met the following criteria were included:

- adult patients (≥ 18 years);
- a histological confirmation of carcinoma of the oropharynx and nasopharynx through biopsy or surgical material;
- exclusive CRT;
- MRI examination for both tumour staging and 3-4 months follow-up after CRT ending;

• DWI and DCE-PWI MRI sequences;
• at least 12 months clinical and cross-sectional imaging follow-up including PET-CT and MRI.
Patients were excluded in case of previous head and neck radiotherapy treatment (4), surgical treatment (5), MRI without both DWI and PWI acquisitions (14), MRI not performed both for tumour staging and follow-up (41), or follow-up less than 12 months (3).
The patients matched our inclusion criteria were 37 (19 males, 18 females) with mean age 59 years (median age 58.5 years, range 36–81 years); 26 patients were affected by oropharyngeal carcinoma (16 HPV positive, 4 HPV negative and 6 unknowns for HPV status) and 11 patients by nasopharyngeal carcinoma). TNM staging (eighth edition of the American Joint Commission on Cancer), HPV status, and the sites of onset of the neoplasms were summarized in Table 1.

MRI protocol- MRI scans for tumour staging and follow-up were performed with a 1.5 T MR Magnetom Aera (Siemens Healthcare, Erlangen, Germany) with devoted head–neck coil. The MRI acquisition protocol was the same for all the examinations, as follows: from 0.9 to 3-mm slice thickness, field of view (FOV) 230 × 200/240 mm, matrix from 230 × 256 to 261 × 484. Unenhanced scans were acquired with
1. sagittal T1-w sampling perfection with application-optimized contrasts using different flip angle evolution (SPACE), repetition time (TR) 500 ms, echo time (TE) 7.2 ms, acceleration factor 2, at axial, coronal, and sagittal multiplanar reconstructions (MPR);
2. sagittal fat-saturated T2-weighted SPACE, TR 3000 ms, TE 380 ms, acceleration factor 2, at axial, coronal, and sagittal MPR;
3. axial T2-weighted turbo spin echo, TR 5050 ms, TE 117 ms, acceleration factor 2, and
4. fat-saturated eco-planar (EPI) DWI (see below).
After gadolinium chelates contrast agent intravenous administration (gadobutrol, Bayer, Germany) 1 ml/10 kg followed by 20 ml saline flush at a rate of 3 ml/s, we acquired
5. axial T1-w turbo spin echo, TR 440 ms, TE 17 ms, acceleration factor 3, and axial T1-w Volumetric Interpolated Breath-hold Examination (VIBE), and
6. Dixon DCE-PWI, TR 10 ms, TE 2.4 ms at axial, coronal, and sagittal MPR (see below).

DWI protocol and post-processing- DWI was obtained by fat-saturated EPI technique, TR 4100 ms, TE 55 ms, and two b values ($b_{50\text{-}800}$ s/mm^2), matrix 102 × 128, and acceleration factor 3. The median ADC value of the primitive tumour and of the residual tissue after CRT was calculated using a workstation (Syngo, Siemens) by positioning three regions of interest (ROI) with an average intratumoral area of 0.30–0.40 cm^2 each on three contiguous axial sections. Cystic areas within solid lesions and necrotic, hemorrhagic or proteinaceous areas on T1 and T2-w sequences were excluded. Median ADC values of the ipsilateral trapezius muscle were also obtained in the same way.

DCE-PWI protocol and post-processing- DCE-PWI was obtained through two VIBE T1-w sequences, 3.5-mm slice thickness, 0.7 interslice gap, FOV 250 × 226 mm, matrix 139 × 192, flip angles 5° and 15°, and acceleration factor 3 for baseline T1-mapping acquisitions. After contrast agent administration, one VIBE T1-w lasting 350 s and with a temporal resolution of 5 s was acquired as follows: TR 4.65 ms, TE 1.66 ms, 3.5-mm slice thickness, FOV 250 × 226.6 mm, matrix 139 × 192, flip angle 30°, acceleration factor 3, and peripheral K space sampling with time to centre 2.2 s.
Time/intensity curve (I/t), AUC and K(trans) values of the primitive tumour and of the residual tissue after CRT were generated by using the IntelliSpace software version 9.0 (Philips, Amsterdam, The Netherlands) from the native DCE-

PWI images by drawing an ROI including at least 50% of the largest lesion section. Vessels, calcifications, necrotic, hemorrhagic, and cystic areas within solid components were excluded. Before lesion sampling, an ROI was placed on the internal carotid artery to obtain the Arterial Input Function curve, defined as the contrast concentration in vessels feeding to tissue at each point in time during the contrast passage. I/t, AUC and K(trans) values of the ipsilateral trapezius muscle were also obtained.

Image Assessment- All MRI examinations were independently reviewed by two radiologists with 12 (CN) and 7 (MP) years of experience in head and neck imaging, respectively. MRI performed both for tumour staging and follow-up 3-4 months after the end of CRT were evaluated for each patient retrieved in the study.
The following morphological, DWI and DCE-PWI MRI features were assessed:
- signal intensity of primitive tumour and residual tissue after CRT (hyper- iso, or hypointense respect to muscle signal) on T2-weighted images;
- maximum size of primitive tumour and submucosal enhancement thickness of residual tissue after CRT on post-contrast T1-weighted images.
- signal intensity of residual tissue after CRT on DWI_{b800} images (hyper- or hypointense);
- median ADC values, AUC and K(trans) values of primitive tumour (ADC_{pre}, AUC_{pre}, and $K(trans)_{pre}$) and residual tissue after CRT (ADC_{post}, AUC_{post}, and $K(trans)_{post}$) on DWI and DCE-PWI MRI sequences, respectively;
- ratio between AUC and K(trans) values of residual tissue after CRT and AUC and K(trans) values of primitive tumour, respectively ($AUC_{post/pre}$ and $K(trans)_{post/pre}$);
- ratio between AUC and K(trans) values of post-CRT residual tissue and primitive tumour, standardized with respect to AUC and K(trans) values of the ipsilateral trapezius muscle ($AUC_{post/pre/muscle}$ and $K(trans)_{post/pre/muscle}$), as follow:

$$\frac{\text{AUCpost}}{\text{AUC muscle post}} : \frac{\text{AUC pre}}{\text{AUC muscle pre}} \text{ and } \frac{\text{K(trans)post}}{\text{K(trans) muscle post}} : \frac{\text{K(trans) pre}}{\text{K(trans) muscle pre}}$$

Where $AUC_{muscle\ pre}$, $AUC_{muscle\ post}$, $K(trans)_{muscle\ pre}$ and $K(trans)_{muscle\ post}$ are AUC and K(trans) values of the ipsilateral trapezius muscle measured on pre-treatment and post-treatment DCE-PWI MRI, respectively.
The diagnosis of tumour response to CRT or tumoral persistence/recurrences was defined on follow-up with clinical examination and cross-sectional imaging including PET-CT for at least 12 months after MRI. Post-treatment biopsy was performed only in patients with positive PET-CT during follow-up. Clinical examination and MRI images were used to validate negative results as true negatives in patients with negative PET-CT during follow-up and without post-treatment biopsy or in patients with negative post-treatment biopsy results. Histology from endoscopic biopsy was performed in case of 12 patients with positive PET-CT (5 tumoral persistence/recurrences and 7 negative biopsy), whereas imaging alone was available in 25 patients with negative PET-CT during follow-up (all post-CRT changes).

Statistical analysis- Quantitative continuous variables are expressed as mean ± standard deviation or median and range, while categorical values are reported as the absolute count and percentage. The interobserver reliability for MRI was calculated using the Cohen kappa coefficient. Kappa values of 0.01–0.20, 0.21–0.40, 0.41–0.60, 0.61–0.80, 0.81–0.99, and 1 represented slight, fair, moderate, substantial, almost perfect, and perfect agreement, respectively.
Data was presented as percentage or as mean (± standard deviation) and median (interquartile range), as appropriate. Continuous variables were tested for normality using Kolmogorov-Smirnov test. The association of each parameter and the status at the follow-up (i.e., tumor persistence/recurrence or post-CRT changes) was tested using the t-Student test or the Mann-Whitney U-test for independent samples, as appropriate. For the parameters with statistically significant

association with the status at the follow-up, a cut-off value to discriminate post-CRT changes with respect to tumor persistence/recurrence was calculated using Receiver Operating Characteristic (ROC) curve analysis. In particular, sensitivity and specificity were calculated for the entire spectrum of values and cut-off values were chosen as the values with the highest sensitivity and specificity at the same time. The area under the ROC curve was considered as a measure of the overall performance of each parameter (diagnostic accuracy) to discriminate the status at the follow-up.

The analyses were performed using the SPSS® v. 27.0 statistical analysis software (IBM Corp., New York, NY; formerly SPSS Inc., Chicago, IL), considering an alfa level of 0.05 as significant.

Results

Table 2,3, 4, and 5 summarized the results of the current study. The Cohen kappa values showed almost perfect agreement between the two observers for tumour size, signal intensity on T2-weighted images and submucosal enhancement of the residual tissue on post-CRT MRI (K value from 0.82 to 0.89), and substantial agreement for DWI and DCE-PWI MRI evaluations (K value from 0.75 to 0.79).

The submucosal enhancement thickness of post-treatment residual tissue was markedly different between post-CRT changes (media 3.3 mm, range 0-10.3 mm) and tumour persistence/recurrence (media 22.7 mm, range 7.2-45.4 mm). A statistically significant difference between patients with post-CRT changes (32) and patients with tumour persistence/recurrence (5) was found for DWI MRI evaluation performed at 3-4 months follow-up. Median (ADC_{post}) was significantly greater in post-CRT alterations ($1.54 \pm 0.23 \times 10^{-3}$ mm^2/s) than in tumour recurrence ($1.05 \pm 0.267 \times 10^{-3}$ mm^2/s). In detecting patients with post-CRT changes, ADC_{post} values > 1.33×10^{-3} mm^2/s had sensitivity 84.6% and specificity 100% (P= 0.002, ROC curve in Figure 1a), a percentage increase > 65.0% among median ADC_{post} values compared to median ADC_{pre} values ($ADC_{post\text{-}pre\%}$) showed sensitivity 76.9% and specificity 75.0% (P= 0.005, ROC curve in Figure1b), and value > 0.72×10^{-3} mm^2/s in the difference between median ADC_{post} and ADC_{pre} values ($ADC_{post\text{-}pre}$) had sensitivity 42.9% and specificity 100% (P= 0.052, ROC curve in Figure 1c). Although bordering on statistical significance, a P-value of 0.052 was considered significant considering the low number of patients with tumour persistence/recurrences. Values > 1.15 and > 0.85 for the ratio between median ADC_{post} values and median ADC values of the trapezius muscle measured in post-treatment MRI images ($ADC_{post/muscle\ post}$) showed sensitivity 80.1% and 96.2%, and specificity 100% and 75.0%, respectively (P= 0.002, ROC curve in Figure 1d).

The signal intensity evaluation on DWI_{b800} images of the residual tissue after CRT showed sensitivity 93.7%, specificity 80.0%, positive predictive value 96.7%, negative predictive value 66.6%, and diagnostic accuracy 91.89%. In particular, DWI_{b800} images showed a hypointense signal intensity in 30 out of 32 patients with post-CRT changes, and in only 1 out of 5 patients with tumour recurrence.

No statistically significant difference between post-CRT changes and tumour recurrence was found for DCE-PWI MRI evaluation performed at 3-4 months follow-up. Mean $AUC_{post/pre/muscle}$ and mean $K(trans)_{post/pre/muscle}$ values were similar in patients with post-CRT alterations (1.09 ± 0.57, range 0.37-2.70; 1.07 ± 0.91, range 0.37-4.01, respectively) compared to patients with tumour recurrence (1.08 ± 0.11, range 0.92-1.18; 1.02 ± 0.11, range 0.86-1.14).

$AUC_{post/pre}$ and $K(trans)_{post/pre}$, the not standardized ratio with respect to AUC and K(trans) values of the ipsilateral trapezius muscle, respectively, were less reproducible than $AUC_{post/pre/muscle}$ and mean $K(trans)_{post/pre/muscle.}$

No significant difference was found in DWI and DCE-PWI values measured on pre-treatment MRI between patients with post-CRT changes and tumour persistence/recurrence at follow-up.

Discussion

DWI MRI evaluation was helpful in distinguishing post-CRT changes from tumour recurrence at 3-4 months follow-up. A statistically significant increase in median ADC_{post} was observed in patients with post-CRT changes, compared to patients with tumour recurrence. $ADC_{post\text{-}pre}$ values > 0.71 x 10 x 3 mm^2/s, $ADC_{post\text{-}pre\%}$ > 65.0%, $ADC_{post/muscle\ post}$ values > 0.85, and hypointense signal intensity on DWI_{b800} images were strongly suggestive for post-CRT changes.

The interpretation of morphological MRI features in our study was in agreement with the criteria described by Alianou, Becker and other authors [6, 28-30]: masslike lesion with moderately high (intermediate) signal intensity on T2-weighted images was suggestive for tumour persistence/recurrences, diffuse lesion with high signal intensity on T2 for post-radiotherapy inflammatory edema, whereas linear or triangular lesion with very low signal intensity on T2 (similar to or lower than that of muscle) for late fibrosis (post-radiotherapy scar). In particular, Alianou et al stated that the combination of morphologic MRI, with clearly defined criteria, and DWI yields superior results than DWI alone [6].

These authors also estimated the grade of enhancement after intravenous gadolinium administration on morphological MRI. Our study, instead, tried to quantify and differentiate, diffusion, perfusion and vessel permeability of primary tumour, tumoral persistence/recurrences, and post-treatment changes on DCE-PWI MRI performed 3-4 months after the end of CRT by measuring ADC, AUC, and K(trans) values.

ADC values are directly proportional to the number and grade of diffusion of water molecules, and extracellular volume. Conversely, the relationship between tumoral tissue, post-treatment alterations and changes in DCE-PWI values is more controversial. As Ktrans reflects the combined effect of plasma blood flow, permeability and capillary surface area, it does not provide insight into which of the constituent factors (variations in permeability or capillary surface area) are responsible for the observed changes [25]. It is possible, however, to state that vascular changes associated with a recurrent tumour represent neoangiogenesis, whereas post-treatment non-tumorous lesions shows vascular changes of continued successful therapy and fibrosis [31].

Fatma et al found statistically different mean ADC values of 1.02 ± 0 .20 $x10^{-3}$ mm^2/s and of 1.42 ± 0.23 $x10^{-3}$ mm^2/s for tongue carcinoma recurrence and post-treatment changes, respectively [32]. These ADC values were similar to those in our study, in which all 32 patients with post-CRT changes showed an increase in post-treatment median ADC values, compared to pre-treatment median ADC values. Post-treatment median ADC values were > 1.4 x 10^{-3} mm^2/s in 24 patients with post-CRT changes (mean 1.56 x 10^{-3} mm^2/s), < 1.4 x 10^{-3} mm^2/s in in the remaining 8 patients with post-CRT changes (mean 1.24 x 10^{-3} mm^2/s, least 0.96 x 10^{-3} mm^2/s), and in all 5 patients with tumour persistence/recurrences (mean 1.05 x 10^{-3} mm^2/s). This partial overlap among the ADC values between post-CRT changes and tumoral recurrence (Figure 2a) was reported in literature. Connor et al found decreased mean ADC values in patients with successful treatment [33], in agreement with other authors [34-36]. Other post-treatment studies, conversely, [30, 37-46] found that increased mean ADC values were predictive of treatment success.

Tshering Vogel et al have shown that major overlap of ADC values limits the ability of quantitative DWI MRI sequence to differentiate tumour recurrences from post-radiotherapy changes [47]. Ailianou et al divided post-therapy changes into two groups, post-radiotherapy edema and later fibrosis, based on signal intensity on T2- and T1-weighted images, and grade of enhancement after intravenous gadolinium administration. They found that mean ADC values in head and neck squamous cell carcinoma (1.09 ± 0.29 x 10^{-3} mm^2/s) was significantly lower ($P < 0.05$) than in post-radiation therapy inflammatory edema (1.75 ± 0.34 x 10^{-3} mm^2/s), with virtually no overlap; however, it was similar to that in late fibrosis (0.98 ± 0.26 x 10^{-3} mm^2/s, P= 0.05). Thus, authors suggested not to group post-radiotherapy changes all together but to distinguish them in post-radiotherapy edema and later fibrosis [6]. These results may justify ADC values overlap between

post-CRT and recurrence observed in our study and previous cites papers, which did not consider this distinction between post-radiotherapy edema and late fibrosis in patients with successful treatment.

FDG-PET is frequently used for treatment response assessment with high sensitivity but lower specificity [48], especially in the first months after treatment due to inflammation, granulation and scar tissue [29]. FDG-PET performed 3-6 months after the end of the treatment was positive in 12 patients of the current study, however, only 5 patients had tumour recurrences at follow-up. Compared to FDG-PET, ADC can be performed earlier to assess treatment response, but false positive and false negatives are not fully excluded [49]. As well known, radiotherapy induced inflammatory edema, which tends to have high ADCs. As oppose, ADCs tend to be low in late fibrosis because is mainly composed of densely packed collagen [6]. Likewise, locoregional failure with tumour recurrence leads to restricted diffusion, due to high tumoral cells density, with a subsequent decrease in ADC [37]. Studies that used ADC values without taking into account the DWI signal intensity, i.e., the presence or absence of restricted diffusion, underestimated the accuracy of diffusion weighted MRI [49]. Scar tissue can display low ADC but normally in combination with lack of diffusion restriction (hypointense signal on high b value DWI images). This distinguishes scar tissue from tumour with low values on the ADC map together with diffusion restriction (hyperintense signal on DWI images) [50].

In the current study, no significant differences were found on DCE-PWI analysis between patients with post-CRT changes and patients with tumour recurrence at 3-4 months follow-up. Patients with post-CRT changes, however, showed more pronounced variations than patients with tumour recurrence in mean $AUC_{post/pre/muscle}$ and mean $K(trans)_{post/pre/muscle}$ values. In particular, the graphic distribution of $AUC_{post/pre/muscle}$ and mean $K(trans)_{post/pre/muscle}$ values (Figure 2b and 2c) clearly divided the study patients into three groups. The first group of patients showed $AUC_{post/pre/muscle}$ and $K(trans)_{post/pre/muscle}$ values < 0.85 (low to 0.37 and 0.30, respectively), the second (central) group of patients had $AUC_{post/pre/muscle}$ and $K(trans)_{post/pre/muscle}$ values ≈ 1 (range 0.85-1.2), and a third group had higher $AUC_{post/pre/muscle}$ and mean $K(trans)_{post/pre/muscle}$ values (up to 2.07 and 4.01, respectively). Interesting, the first and third groups consisted only of successfully treated patients, and all 5 patients with tumour recurrence belonged to the second group. Only few successful treated patients showed similar $AUC_{post/pre/muscle}$ and $K(trans)_{post/pre/muscle}$ values compared to patients with tumour persistence/recurrences values (Figure 3-4). Post-treatment changes may lead to significant variations in DCE-PWI parameters values since K(trans) may be sensitive to angiogenic modifications [25] (Figure 5-6). Therefore, although with some degree of overlap, little or no changes in $AUC_{post/pre/muscle}$ and mean $K(trans)_{post/pre/muscle}$ values, and therefore in tumoral neoangiogenesis, may be considered a post-treatment indicator of tumour persistence/recurrences (Figure 7-8). As for DWI, the aforementioned variations of the DCE-PWI values could reflect the different tissue component, mainly inflammatory or fibrotic, of the post-treatment changes. CRT induce an acute response with release of tumour growth factor as primary mediator and cytokines that leads to inflammation, followed by fibroblast recruitment and activation with extracellular matrix deposition. This inflammatory process ultimately evolves into a fibrotic one characterized by increased collagen deposition, poor vascularity, and scarring (Figure 9-10). It is also reasonable to argue that the late effects of radiation vary depending on the radiation dose, fraction size, and volume treated, and may be influenced by the radiosensitivity of individual patients [51].

In the current study, pre-treatment DWI and DCE-PWI MRI was not useful in predicting tumour response to CRT; this result was not in agreement with the paper written by Ng et al. They found that pretreatment K(trans) of the primary tumour was a significant predictor of local failure of oropharyngeal and hypopharyngeal carcinoma treated with CRT [52].

Some limitations need to be mentioned. The relationship between multiparametric functional MRI and HNSCC stage, neck lymph node metastasis, histological tumour grading, progression-free survival, HPV status, intravoxel incoherent

motion, or tumoral 18F-FDG-PET standard uptake value (SUV) were not performed. Zhang et al. [53] found statistically significant higher ADC values in locally advanced nasopharyngeal carcinoma (T3/T4) in comparison to early-stage tumours (T1/T2). Zheng et al reported that DCE parameters correlated well with tumour stage in nasopharyngeal carcinoma [54]. Conversely, Leifels et al. did not find significant differences in DWI and DCE-PWI parameters between T1/2 and T3/4 HNSCC; they demonstrated, however, a strong correlation between high K(ep) values, N2 stage, and microvessel density in HNSC suggesting that tumour microvessel density might influence lymphatic metastatic spread in HNSCC [55]. Choi et al. mentioned that poorly differentiated tumours had statistically significant lower ADC values than G1/G2 tumours [56]. Fruehwald-Pallamar, however, reported that ADC values could not distinguish tumour stages [57]. Several parameters of tumour perfusion, diffusion, and glucose metabolism were associated together in previous work literature, but results are controversial. Bisdas et al. identified significant correlations between SUV values DCE-PWI parameters [58], whereas the study of Nakajo et al. showed a statistically significant inverse correlation between SUV and mean ADC [59]. However, other authors did not identify significant correlations between DWI, DCE-PWI, and glucose metabolism [58-60]. Leifels at. found that ADC_{mean} correlated slightly with K(trans) (P= 0.04) [55], whereas for Covello et al. ADC_{mean} correlated inversely with K(trans) [61].

Another limitation was the relative low sample size of our study. Nevertheless, most papers regarding HNSCC and functional MRI do not consider both DWI and DCE-PWI for therapy assessment or did not include both pre- and post-treatment MRI; moreover, to our knowledge, few papers in literature exclusively recruited patients with pharyngeal cancer [11, 33, 52], and only one of this was performed with both DWI and DCE-PWI [11]. The small number of patients with tumour persistence/recurrences in the current study (5) has been related to the well-known excellent response to CRT treatment in most cases of oropharyngeal, especially if HPV positive, and nasopharyngeal carcinomas.

Then, our single-center results may not be generalizable until more evidence is gathered.

To summaries, the role of multiparametric investigation of HNSCC currently is an up-to-date debate, and data reported in literature are controversial presumably due to tumour heterogeneity [55]. The analysis of possible relationships between microcirculation, cellularity, and other tissue and metabolic features, however, may have significant clinical implications such as in guidance for treatment planning, early prediction of treatment responses, indication to perform biopsy in the early follow-up, and evaluation of treatment outcome [17, 62]. Therefore, strictly MRI morphologic evaluation, i.e signal intensity on T1- and T2-weighted images and grade of enhancement is mandatory in HNSCC, and further studies are needed to establish whether or not multiparametric investigation could be used successfully in clinical daily practice.

Conclusion

Functional MRI imaging with both DWI and DCE-PWI sequences, in association with morphological criteria, was useful in the distinction between post-CRT treatment changes and tumoral recurrence in patients affected by primary nasopharyngeal and oropharyngeal carcinoma. ADC_{post} values > 1.33 x 10^{-3} mm^2/s and $ADC_{post\text{-}pre}$ values > 0.72 x 10^{-3} mm^2/s identified patients with post-CRT changes with excellent specificity (100%). For $AUC_{post/pre/muscle}$ and $K(trans)_{post/pre/muscle}$, values < 0.85 were suggestive for fibrosis, values ≈1 (range 0.85-1.2) were found in tumoral persistence/recurrence, and higher values indicated post-CRT inflammatory edema.

In the current work no significant difference was found in DWI and DCE-PWI values measured on pre-treatment MRI between patients with post-CRT changes and tumour persistence/recurrence. Further studies are needed to evaluate the usefulness of pre-treatment DWI and DCE-PWI MRI in predicting tumour response to CRT.

References

1. Parkin DM, Bray F, Ferlay J, et al. (2005) Global cancer statistics, 2002. CA Cancer J Clin.;55(2):74–108
2. Mungai F, Verrone GB, Pietragalla M et al. (2019) CT assessment of tumor heterogeneity and the potential for the prediction of human papillomavirus status in oropharyngeal squamous cell carcinoma. Radiol Med. Sep;124(9):804-811
3. Jajodia A, Aggarwal D, Chaturvedi AK et al. (2019) Value of diffusion MR imaging in differentiation of recurrent head and neck malignancies from post treatment changes. Oral Oncol. Sep;96:89-96
4. Overgaard J (2011) Hypoxic modification of radiotherapy in squamous cell carcinoma of the head and neck- a systematic review and meta-analysis. Radiother. Oncol. 100, 22–32
5. Brockstein B, Haraf DJ, Rademaker AW et al (2004) Patterns of failure, prognostic factors and survival in locoregionally advanced head and neck cancer treated with concomitant chemoradiotherapy: a 9-year, 337-patient, multi-institutional experience. Ann Oncol 15(8):1179–1186
6. Ailianou A, Mundada P, De Perrot T, Pusztaszieri M, Poletti PA, Becker M (2018) MRI with DWI for the Detection of Posttreatment Head and Neck Squamous Cell Carcinoma: Why Morphologic MRI Criteria Matter. AJNR Am J Neuroradiol. Apr;39(4):748-755
7. Chang JH, Wu CC, Yuan KSP, Wu ATH, Wu SY (2017) Loco-regionally recurrent head and neck squamous cell carcinoma: incidence, survival, prognostic factors and treatment outcomes. Oncotarget 8:55600–55612
8. King AD, Thoeny HC (2016) Functional MRI for the prediction of treatment response in head and neck squamous cell carcinoma: potential and limitations. Cancer Imaging 16:23
9. Teicher BA (1994) Hypoxia and drug resistance. Cancer Metastasis Rev. 13, 139–68
10. Mukherji SK, Wolf GT (2003) Evaluation of head and neck squamous cell carcinoma after treatment. AJNR Am J Neuroradiol 24(9):1743–6
11. Martens RM, Koopman T, Lavini C et al (2021) Multiparametric functional MRI and 18F-FDG-PET for survival prediction in patients with head and neck squamous cell carcinoma treated with (chemo)radiation Eur Radiol. Feb;31(2):616-628
12. Gaddikeri S, Gaddikeri RS, Tailor T et al. (2016) Dynamic Contrast-Enhanced MR Imaging in Head and Neck Cancer: Techniques and Clinical Applications. AJNR Am J Neuroradiol 37(4):588-95
13. Bernstein JM, Homer JJ, West CM (2014) Dynamic contrast-enhanced magnetic resonance imaging biomarkers in head and neck cancer: Potential to guide treatment? A systematic review. Oral Oncol. 50, 963–970
14. Mehanna H, Wong WL, McConkey C et al (2016) PET-CT surveillance versus neck dissection in advanced head and neck cancer. N Engl J Med 374:1444–1454
15. Meyer HJ, Leifels L, Schob S, Garnov N, Surov A (2018) Histogram analysis parameters identify multiple associations between DWI and DCE MRI in head and neck squamous cell carcinoma. Magn Reson Imaging. Jan;45:72-77
16. Maraghelli D, Pietragalla M, Cordopatri C et al. (2021) Magnetic resonance imaging of salivary gland tumours: Key findings for imaging characterisation. Eur J Radiol. Jun;139:109716
17. Han M, Kim SY, Lee SJ, Choi JW (2015) The Correlations Between MRI Perfusion, Diffusion Parameters, and 18F-FDG PET Metabolic Parameters in Primary Head-and-Neck Cancer: A Cross-Sectional Analysis in Single Institute. Medicine (Baltimore) 94 (2015) e2141

18. Surov A, Stumpp P, Meyer HJ et al. (2016) Simultaneous (18)F-FDG-PET/MRI: Associations between diffusion, glucose metabolism and histopathological parameters in patients with head and neck squamous cell carcinoma. Oral. Oncol. 58 14-20
19. Nardi C, Tomei M, Pietragalla M et al. (2021) Texture analysis in the characterization of parotid salivary gland lesions: A study on MR diffusion weighted imaging. Eur J Radiol. Mar;136:109529
20. Pietragalla M, Nardi C, Bonasera L et al. (2020) The role of diffusion-weighted and dynamic contrast enhancement perfusion-weighted imaging in the evaluation of salivary glands neoplasms. Radiol Med. Sep;125(9):851-863
21. Baliyan V, Das CJ, Sharma R et al (2016) Diffusion weighted imaging: Technique and applications. World J. Radiol. 8, 785–798
22. Mungai F, Verrone GB, Bonasera L et al. (2021) Imaging biomarkers in the diagnosis of salivary gland tumors: the value of lesion/parenchyma ratio of perfusion-MR pharmacokinetic parameters. Radiol Med. Jun 28
23. Rajabi M, Mousa SA (2017) The Role of Angiogenesis in Cancer Treatment. Biomedicines 5, 34
24. Kabadi SJ, Fatterpekar G, Anzai Y et al (2018) Dynamic Contrast-Enhanced MR Imaging in Head and Neck Cancer. Magn. Reson. Imaging Clin. N. Am. 26, 135–149
25. Petralia G, Summers PE, Agostini A et al. (2020) Dynamic contrast-enhanced MRI in oncology: how we do it. Radiol Med. Dec;125(12):1288-1300
26. Connolly M, Srinivasan A (2018) Diffusion-Weighted Imaging in Head and Neck Cancer: Technique, Limitations, and Applications. Magn. Reson. Imaging Clin. N. Am. 26, 121–133
27. Malayeri AA, El Khouli R, Zaheer A et al (2011) Principles and Applications of Diffusion- weighted Imaging in Cancer Detection, Staging, and Treatment Follow-up. RadioGraphics 31, 1773–1791
28. Becker M, Varoquaux AD, Combescure C, et al. Local recurrence of squamous cell carcinoma of the head and neck after radio(chemo)therapy: diagnostic performance of FDG-PET/ MRI with diffusion-weighted sequences. Eur Radiol 2018;28: 651– 63 CrossRef Medline
29. Varoquaux A, Rager O, Dulguerov P, et al (2015) Diffusion-weighted and PET/MR imaging after radiation therapy for malignant head and neck tumors. Radiographics 35:1502–27 CrossRef Medline
30. King AD, Keung CK, Yu KH, et al (2013) T2-weighted MR imaging early after chemoradiotherapy to evaluate treatment response in head and neck squamous cell carcinoma. AJNR Am J Neuroradiol 34:1237– 41 CrossRef Medline
31. El Beltagi AH, Elsotouhy AH, Own AM, Abdelfattah W, Nair K, Vattoth S (2019) Functional magnetic resonance imaging of head and neck cancer: Performance and potential. Neuroradiol J. Feb;32(1):36-52
32. Fatma MS (2020) Value of Diffusion-Weighted and Perfusion-Weighted MR Imaging in Differentiation of Recurrent Tongue Carcinoma from Post-Treatment Changes. The Medical Journal of Cairo University. 88. 1893-1902
33. Connor S, Sit C, Anjari M et al (2021). The ability of post-chemoradiotherapy DWI ADCmean and 18F-FDG SUVmax to predict treatment outcomes in head and neck cancer: impact of human papilloma virus oropharyngeal cancer status. J Cancer Res Clin Oncol. Aug;147(8):2323-2336
34. Galbán CJ, Lemasson L, Hoff BA et al (2015) Development of a multiparametric voxel-based magnetic resonance imaging biomarker for early cancer therapeutic response assessment. Tomography 1:44–52

35. Wong KH, Panek R, Welsh L et al (2016) The predictive value of early assessment after 1 cycle of induction chemotherapy with 18F- FDG PET/CT and diffusion-weighted MRI for response to radical chemoradiotherapy in head and neck squamous cell carcinoma. J Nucl Med 57:1843–1850
36. Paudyal R, Hun J, Riaz N et al (2017) Intravoxel incoherent motion diffusion-weighted MRI during chemoradiation therapy to characterize and monitor treatment response in human papillomavirus head and neck squamous cell carcinoma. JMRI 45:1013–1023
37. King AD, Chow KK, Yu KH, et al. (2013) Head and neck squamous cell carcinoma: diagnostic performance of diffusion-weighted MR imaging for the prediction of treatment response. Radiology 266: 531–538
38. King AD, Mo FK, Yu KH et al (2010) Squamous cell carcinoma of the head and neck: diffusion-weighted MR imaging for prediction and monitoring of treatment response. Eur Radiol 20:2213–2220
39. Vandecaveye V, Dirix P, De Keyzer F et al (2012) Diffusion-weighted magnetic resonance imaging early after chemoradiotherapy to monitor treatment response in head-and-neck squamous cell carcinoma. Int J Radiat Oncol Biol Phys 82:1098–1107
40. Brenet E, Barbe C, Hoeffel C et al (2020) Predictive value of early post-treatment diffusion-weighted MRI for recurrence or tumor progression of head and neck squamous cell carcinoma treated with chemo-radiotherapy. Cancer 12:1234
41. Kim S, Loevner L, Quon H et al (2009) Diffusion-weighted magnetic resonance imaging for predicting and detecting early response to chemoradiation therapy of squamous cell carcinomas of the head and neck. Clin Cancer Res 15:986–994
42. Berrak S, Chawla S, Kim S et al (2011) Diffusion weighted imaging in predicting progression free survival in patients with squamous cell carcinomas of the head and neck treated with induction chemotherapy. Acad Radiol 18:1225–1232
43. Cao Y, Aryal M, Li P et al (2019) Predictive values of MRI and PET derived quantitative parameters for patterns of failure in both p16+ and p16- high risk head and neck cancer. Front Oncol 14:1118
44. Matoba M, Tuji H, Shimode Y et al (2014) Fractional change in apparent diffusion coefficient as an imaging biomarker for predicting treatment response in head and neck cancer treated with chemo- radiotherapy. AJNR Am J Neuroradiol 35:379–385
45. Marzi S, Piludu F, Sanguineti G et al (2017) The prediction of the treatment response of cervical nodes using intravoxel incoherent motion diffusion-weighted imaging. Eur J Radiol 92:93–102
46. Ding Y, Hazle JD, Mohamed ASR et al (2015) Intravoxel incoherent motion imaging kinetics during chemoradiotherapy for human papillomavirus-associated squamous cell carcinoma of the oropharynx: preliminary results form a prospective pilot study. NMR Biomed 28:1645–1654
47. Tshering Vogel DW, Zbaeren P, Geretschlaeger A, et al (2013) Diffusion- weighted MR imaging including bi-exponential fitting for the detection of recurrent or residual tumour after (chemo)radiotherapy for laryngeal and hypopharyngeal cancers. Eur Radiol 2013;23: 562– 69 CrossRef Medline
48. Sheikhbahaei S, Taghipour M, Ahmad R, Fakhry C, Kiess AP, Chung CH, et al. Diagnostic accuracy of follow-up FDG PET or PET/CT in patients with head and neck cancer after definitive treatment: A systematic review and meta-analysis. AJR Am J Roentgenol 2015; 205(3):629–639
49. Van der Hoorn A, van Laar PJ, Holtman GA, Westerlaan HE (2017) Diagnostic accuracy of magnetic resonance imaging techniques for treatment response evaluation in patients with head and neck tumors, a systematic review and meta-analysis. PLoS One. May 24;12(5):e0177986

50. Hustinx R, Lucignani G (2010) PET/CT in head and neck cancer: an update. Eur J Nucl Med Mol Imaging 37(3):645–651
51. Straub JM, New J, Hamilton CD, Lominska C, Shnayder Y, Thomas SM (2015) Radiation-induced fibrosis: mechanisms and implications for therapy. J Cancer Res Clin Oncol. Nov;141(11):1985-94
52. Ng SH, CY Lin, SC Chan et al (2013) Dynamic contrast-enhanced MR imaging predicts local control in oropharyngeal or hypopharyngeal squamous cell carcinoma treated with chemoradiotherapy. PLoS One. Aug 7;8(8):e72230
53. Zhang Y, Liu X, Zhang Y et al. (2015) Prognostic value of the primary lesion apparent diffusion coefficient (ADC) in nasopharyngeal carcinoma: a retrospective study of 541 cases. Scientific Reports, vol. 5, Article ID 12242
54. Zheng D, Chen Y, Chenetal Y (2014) Dynamic contrast-enhanced MRI of nasopharyngeal carcinoma: a preliminary study of the correlations between quantitative parameters and clinical stage," Journal of Magnetic Resonance Imaging, vol. 39, no. 4, pp. 940–948
55. Leifels L, Purz S, Stumpp P et al. (2017) Associations between 18F-FDG-PET, DWI, and DCE Parameters in Patients with Head and Neck Squamous Cell Carcinoma Depend on Tumor Grading. Contrast Media Mol Imaging. Oct 19;2017:5369625
56. Choi SH, Paeng JC, Sohn CH et al. (2011) Correlation of 18F- FDG uptake with apparent diffusion coefficient ratio measured on standard and high b value diffusion MRI in head and neck cancer. Journal of Nuclear Medicine, vol. 52, no. 7, pp. 1056–1062
57. Fruehwald-Pallamar J, Czerny C, Mayerhoefer ME et al. (2011) Functional imaging in head and neck squamous cell carcinoma: correlation of PET/CT and diffusion-weighted imaging at 3 Tesla. European Journal of Nuclear Medicine and Molecular Imaging, vol. 38, no. 6, pp. 1009–1019
58. S. Bisdas, O. Seitz, M. Middendorp et al. (2010) An exploratory pilot study into the association between microcirculatory parameters derived by MRI-based pharmacokinetic analysis and glucose utilization estimated by PET-CT imaging in head and neck cancer. European Radiology, vol. 20, no. 10, pp. 2358–2366
59. Nakajo M, Nakajo M, Kajiya Y et al. (2012) "FDG PET/CT and diffusion-weighted imaging of head and neck squamous cell carcinoma: comparison of prognostic significance between primary tumor standardized uptake value and apparent diffusion coefficient," Clinical Nuclear Medicine, vol. 37, no. 5, pp. 475– 480
60. Rasmussen JH, Nørgaard M, Hansen AE et al. (2017) Feasibility of multiparametric imaging with PET/MR in head and neck Squamous cell carcinoma. Journal of Nuclear Medicine, vol. 58, no. 1, pp. 69–74
61. Covello M, Cavaliere C, Aiello M et al. (2015) Simultaneous PET/ MR head-neck cancer imaging: preliminary clinical experience and multiparametric evaluation," European Journal of Radiology, vol. 84, no. 7, pp. 1269–1276
62. Gawlitza M, Purz S, Kubiessa K et al. (2015) "In vivo correlation of glucose metabolism, cell density and microcirculatory parameters in patients with head and neck cancer: initial results using simultaneous PET/MRI," PLoS ONE, vol. 10, no. 8, Article ID e0134749

Tables

Patients	Sex	Age	Tumour site	HPV status	TNM 8th	Tumour stage	Follow-up
1	F	63	O	P	T2N1M0	I	RT C
2	M	48	N	U	T4N2M0	IVA	RT C
3	F	72	O	U	T3N0M0	III	RT C
4	M	72	O	P	T2N1M0	I	RT C
5	M	61	O	U	T4aN2bM0	IVA	RT C
6	F	36	N	U	T2aN1M0	IIB	RT C
7	F	52	N	Ne	T1N0M0	I	PT
8	M	81	O	P	T1N1M0	I	RT C
9	M	57	N	Ne	T1N2M0	III	RT C
10	F	58	O	U	T4aN1M0	IVA	RT C
11	M	59	N	U	T2bN2M0	III	RT C
12	M	68	O	P	T1N1M0	I	RT C
13	M	58	O	P	T1N1M0	I	RT C
14	F	63	O	P	T2N1M0	I	RT C
15	M	75	O	P	T1N1M0	I	RT C
16	F	57	O	P	T1N1M0	I	RT C
17	M	37	N	U	T2aN3M0	IVB	RT C
18	F	51	O	P	T2N1M0	I	RT C
19	M	61	O	U	T4aN1M0	IVA	RT C
20	M	57	O	P	T2N1M0	I	RT C
21	F	52	N	U	T1N1M0	IIB	RT C
22	M	67	O	Ne	T4aN0M0	IVA	RT C
23	F	65	O	U	T3N1M0	III	RT C
24	M	58	N	U	T3N3M1	IVC	PT
25	F	63	N	Ne	T4N2M0	IVA	RT C
26	F	55	O	U	T4aN1M0	IVA	PT
27	F	47	O	P	T4N1M0	II	RT C
28	M	61	O	P	T1N2M0	II	RT C
29	F	47	O	Ne	T4aN2M0	IVA	PT
30	F	69	O	P	T2N1M0	I	RT C
31	M	41	O	P	T1N1M0	I	RT C
32	M	52	N	U	T2N0M0	IIA	RT C
33	F	55	O	P	T1N1M0	I	RT C
34	M	63	O	Ne	T3N1M0	III	PT
35	F	58	N	U	T2N2M0	III	RT C
36	F	39	O	P	T2N1M0	I	RT C
37	M	56	O	P	T2N1M0	I	RT C

Table 1. Patients' data retrieved in the study.
M: male; F: female; O: oropharynx; N: nasopharynx; P: positive; Ne: negative; U: unknown; RT C: post-radiotherapy changes; T: tumoral persistence/recurrence.
TNM staging eighth edition of the American Joint Commission on Cancer.

Patients	Tumour maximum size (mm)	Tumour median ADC value ($x10^{-3}$ mm^2/s) [ADCpre]	Ipsilateral trapezius muscle median ADC value ($x10^{-3}$ mm^2/s) [ADCmuscle pre]	ADCpre/muscle pre	Tumour AUC value [AUCpre]	Ipsilateral trapezius muscle AUC [AUCmuscle pre]	AUC pre/muscle pre	Tumour K(trans) value (x 10^{-3} min) [K(trans)pre]	Ipsilateral trapezius muscle K(trans) [K(trans) muscle pre]	K(trans) pre/muscle pre
1	15	0.985	1.232	0.8	157.64	35.65	4.42	357.83	46.41	7.71
2	17	0.746	1.235	0.6	58.74	8.97	6.55	78.22	20.2	3.872
3	40	1.136	1.147	1	99.44	21.5	4.63	786.3	93.28	8.429
4	13	0.749	1.435	0.5	146.75	27.02	5.43	347.44	48.55	7.712
5	32	0.674	1.245	0.5	57.39	18.31	3.13	726.74	122	5.956
6	15	0.732	1.456	0.5	80.81	52.73	1.53	105.12	68.92	1.525
7	30	0.921	1.263	0.7	55.66	17.63	3.16	167.5	39.13	4.28
8	15	1.143	1.236	0.9	83.51	36.02	2.31	493.01	38.97	12.929
9	15	0.568	1.162	0.5	76.38	27.16	2.81	231.07	37.05	5.75
10	20	1.044	1.246	0.8	190.12	38.54	4.93	493.36	115.59	4.268
11	14	0.764	1.133	0.7	70.31	40.85	1.72	354.09	174.07	2.034
12	10	0.933	1.151	0.8	44.71	9.07	4.93	79.71	14.54	5.482
13	18	0.742	1.222	0.6	79.62	18.1	4.39	275.87	44.61	6.184
14	15	0.724	1.132	0.6	78.04	25.02	3.11	92.84	15.65	5.932
15	24	0.642	1.111	0.6	56.36	15.82	3.56	375.88	93.92	4.002
16	14	0.76	1.24	0.6	70.33	35.12	2	79.79	40.63	1.963
17	12	0.721	1.243	0.6	49.57	19.47	2.54	141.65	34.56	4.098
18	17	0.861	1.124	0.8	103.94	24.68	4.21	135.98	23.63	5.754
19	20	0.974	1.221	0.9	100.99	15.99	6.73	159.62	13.76	11.6
20	11	0.834	1.342	0.6	213.73	47.41	4.5	331.72	41.46	8
21	13	0.657	1.23	0.5	116.34	50.28	2.31	134	44.23	3.029
22	20	0.991	1.138	0.9	70.71	12.79	5.52	391.55	37.2	10.525
23	17	0.96	0.954	1	147.01	29	5.06	269.13	45.89	5.917
24	7	1.001	1.225	0.8	159.7	45.9	3.46	231.28	49.19	4.701
25	21	0.787	1.173	0.7	128.12	68.04	1.88	173.49	74.38	2.332
26	22	0.805	1.232	0.6	90.94	24.12	3.77	113.35	21.67	5.23
27	35	0.793	1.263	0.6	51.8	21.54	2.42	61.39	12.76	4.811
28	17	0.877	1.095	0.8	113.87	35.4	3.21	128.46	32.45	3.958
29	23	0.834	1.167	0.7	100.14	16.98	5.89	117.63	24.86	4.731
30	20	0.744	1.188	0.6	69.72	28.58	2.43	80.56	32.24	2.498
31	14	1.032	1.152	0.9	82.51	35.02	2.35	488.01	39.97	12.209
32	12	0.756	1.206	0.6	78.38	29.16	2.68	230.07	36.05	6.38
33	8	0.945	1.113	0.8	188.22	36.54	5.15	470.36	113.59	4.140
34	23	0.812	1.181	0.7	100.38	17.18	5.84	118.70	25.68	4.62
35	32	0.688	1.202	0.6	71.41	41.35	1.72	355.19	174.57	2.034
36	15	0.902	1.232	0.7	42.71	8.95	4.77	78.81	14.77	5.33
37	17	0.755	1.117	0.7	79.69	18.2	4.37	273.82	44.31	6.179

Table 2. Pre-treatment patients's data.
ADC: apparent diffusion coefficient; AUC: area under the curve.

Patients	Submucosal contrast enhancement thickness (mm)	T2 signal intensity	DWI b800 signal intensity	Residual tissue median ADC value ($x10^{-3}$ mm^2/s) [ADCpost]	Ipsilateral trapezius muscle median ADC value ($x10^{-3}$ mm^2/s) [ADCmuscle post]	ADCpost/muscle post	Residual tissue AUC value [AUCpost]	Ipsilateral trapezius muscle AUC [AUCmuscle post]	AUCpost/muscle post	Residual tissue K(trans) value ($x\ 10^{-3}$ min) [K(trans)post]	Ipsilateral trapezius muscle K(trans) [K(trans) muscle post]	K(trans) post/muscle post
1	0	Hyper ++	Ipo	1.75	1.232	1.4	89.67	26.87	3.33	176.87	33.21	5.325
2	3	Hyper +	Ipo	1.766	1.321	1.3	35.37	10	3.54	72.4	21.75	3.328
3	10	Hyper +	Ipo	1.604	1.147	1.4	216.24	44.49	4.86	97.82	20.16	4.852
4	0	Ipo	Ipo	1.477	1.257	1.2	61.72	30.2	2.04	31.33	11.33	2.765
5	10	Ipo	Ipo	1.339	1.123	1.2	83.73	29.83	2.8	223.99	115.13	1.945
6	5	Hyper ++	Hyper	1.534	1.324	1.2	88.04	21.38	4.11	595.25	123.07	4.836
7	27	Hyper +	Hyper	1.245	1.623	0.8	59.77	17	3.52	128.1	28.1	4.558
8	0	Ipo	Ipo	1.449	1.128	1.3	188.77	57.9	3.26	422	28.56	14.775
9	6	Hyper ++	Ipo	1.759	1.135	1.5	117.93	19.41	6.07	590.69	25.6	23.07
10	10	Hyper ++	Hyper	1.356	1.234	1.1	96.93	28.33	3.42	77.54	11.8	6.571
11	6	Hyper +	Ipo	1.488	1.221	1.2	51.66	23.35	2.21	87.95	50.84	1.729
12	0	Hyper ++	Ipo	1.34	1.139	1.2	108.56	18.08	6	76.41	8.46	9.031
13	9	Ipo	Ipo	1.661	1.324	1.3	63.53	13.99	4.54	787.92	153.73	5.125
14	0	Ipo	Ipo	1.442	1.232	1.2	98.93	51.03	1.93	48.36	26.49	1.825
15	10	Ipo	Ipo	1.655	1.212	1.4	96.45	18.51	5.21	25.54	7.02	3.368
16	0	Hyper ++	Ipo	1.717	1.321	1.3	152	50.91	2.98	202	55.45	3.642
17	0	Hyper ++	Ipo	1.312	1.353	0.9	94.94	29.88	3.17	121.81	27.22	4.475
18	0	Ipo	Ipo	1.758	1.22	1.4	84.58	28.29	2.98	87.43	26.93	3.246
19	3	Hyper ++	Ipo	1.616	1.374	1.2	123.78	29.15	4.24	122.78	24.54	5.003
20	4	Hyper ++	Ipo	1.963	1.358	1.4	123.66	28.29	4.37	107.65	23.14	4.652
21	0	Hyper +	Ipo	1.322	1.33	1	63.5	55.8	1.13	57.69	49.01	1.177
22	0	Hyper ++	Ipo	1.688	1.13	1.5	68.12	19.89	3.42	65.91	14.61	4.511
23	0	Hyper ++	Ipo	1.831	1.238	1.5	124.21	40.89	3.03	139.23	41.63	3.344
24	12	Hyper +	Hyper	0.874	1.054	0.8	161.98	40.89	3.96	169.92	41.57	4.087
25	0	Hyper ++	Ipo	1.116	1.124	0.9	91.76	39.95	2.29	79.22	41.77	1.896
26	7	Hyper +	Ipo	1.328	1.225	1.1	162.9	36.29	4.48	215.45	39.89	5.401
27	10	Hyper +	Ipo	0.961	1.171	0.8	80.58	18.57	4.33	37.29	7.08	5.266
28	0	Hyper ++	Ipo	1.547	1.286	1.2	67.22	28.01	2.39	30.41	11.15	2.272
29	45	Hyper +	Hyper	0.788	1.013	0.8	109.85	20.23	5.43	56.24	10.39	5.412
30	0	Hyper ++	Ipo	1.726	1.21	1.4	260.88	54.36	4.79	361.56	59.11	6.116
31	0	Ipo	Ipo	1.459	1.138	1.3	59.97	17.12	3.50	421.19	28.04	15.02
32	5	Hyper ++	Ipo	1.769	1.145	1.5	189.77	58.9	3.22	582.68	25.41	22.93
33	11	Hyper ++	Ipo	1.346	1.224	1.1	118.01	19.96	5.91	77.94	11.9	6.54
34	42	Hyper +	Hyper	0.797	1.014	0.8	111.83	21.33	5.24	59.27	12.07	4.91
35	7	Ipo	Ipo	1.498	1.231	1.2	51.40	23.31	2,20	87.05	50.04	1.74
36	0	Hyper ++	Ipo	1.44	1.239	1.2	109.03	18.18	5.99	78.43	9.57	8.19
37	8	Hyper ++	Ipo	1.681	1.344	1.2	63.57	14.02	4.53	780.92	150.73	5.18

Table 3. Post-treatment patients's data.
T2 signal intensity is referred with respect to muscle. Ipo: lower than muscle; Hyper+: similar or slightly higher than muscle; Higher ++: clearly higher than muscle.

Patients	ADCpost-pre	ADCpost-pre%	AUCpost/pre	AUCpost/pre/muscle	K(trans)post/pre	K(trans)post/pre/muscle
1	0,8	77	0.6	0.75	0.494	0.69
2	1	134	0.6	0.5	0.925	0.859
3	0.47	40	2.2	1	0.124	0.575
4	0.73	100	0.4	0.37	0.09	0.358
5	0.66	100	1.45	0.9	0.308	0.326
6	0.6	110	1.08	2.7	5.66	3.171
7	0.7	36	1.07	1.1	0.764	1.064
8	0.3	27	2.26	1.41	0.855	1.142
9	1.2	209	1.53	2.2	2.556	4.012
10	0.3	31	0.5	0.7	0.157	1.539
11	0.7	96	0.6	1.3	0.24	0.85
12	0.4	43	2.4	1.2	0.958	1.647
13	0.9	124	0.8	1.03	2.856	0.828
14	0.7	100	1.3	0.6	0.52	0.307
15	1	159	1.7	1.4	0.06	0.841
16	0.95	125	2.16	1.5	2.531	1.855
17	0.59	82	1.91	1.24	0.859	1.091
18	0.89	103	0.81	0.7	0.567	0.564
19	0.64	66	1.22	0.63	0.769	0.431
20	1.13	136	0.57	1	0.324	0.581
21	0.67	103	0.54	0.5	0.43	0.388
22	0.69	70	0.96	0.61	0.168	0.428
23	0,87	90	0.84	0.6	0.517	0.565
24	-0.13	-13	1.01	1.14	0.734	0.869
25	0.33	42	0.71	1.21	0.456	0.813
26	0.52	65	1.8	1.18	1.900	1.032
27	0.16	21	1.5	1.79	0.607	1.094
28	0.67	76	0.6	0.74	0.236	0.574
29	-0.04	-5	1.1	0.92	0.478	1.143
30	0.98	131	3.7	1.97	4.488	2.448
31	0.43	41	0.73	1.49	0.86	2.448
32	1.01	134	2.42	1.20	2.532	3.594
33	0.40	42	0.63	1.15	0.165	1.579
34	-0.01	-1	1.11	0.90	0.499	1.062
35	0.81	118	0.72	1.28	0.245	0.855
36	0.54	60	2.55	1.25	0.995	1.536
37	0.93	123	0.80	1.04	2.851	0.838

Table 4. Comparison between post-treatment and pre-treatment patients's data.
ADCpost-pre: residual tissue median ADC value - tumour median ADC value.
ADCpost-pre%: residual tissue median ADC value - tumour median ADC value%.
AUCpost/pre: ratio between residual tissue AUC and tumour AUC value.
AUCpost/pre/muscle: ratio between residual tissue AUC and tumour AUC value, standardized with respect to AUC values of the ipsilateral trapezius muscle.
K(trans)post/pre: ratio between residual tissue K(trans) value and tumour K(trans) value.
K(trans)post/pre/muscle: ratio between residual tissue K(trans) value and tumour K(trans) value, standardized with respect to K(trans) values of the ipsilateral trapezius muscle.

Magnetic resonance features	Residual tissue (32)	Tumour persistence/recurrences (5)	P-value
Pre-treatment tumour maximum size (mm)	18.46 ± 7.223 (10 – 40)	20.50 ± 9.678 (7 – 30)	0.391
Pre-treatment tumour median ADC value (x10^{-3} mm^2/s) [ADCpre]	0.828 ± 0.151 (0.568 – 1.143)	0.890 ± 0.088 (0.805 – 1.001)	0.245
Pre-treatment tumour AUC value [AUCpre]	96.767 ± 44.157 (44.71 – 213.73)	101.61 ± 43.212 (55.66 – 159.70)	0.746
Pre-treatment tumour K(trans) value (x 10^{-3} min) [K(trans)pre]	264.800 ± 196.757 (61.39 – 786.30)	157.440 ± 55.022 (113.35 – 231.28)	0.498
ADCpre/trapezius muscle ADC pre-treatment value	0.69 ± 0.160 (0.5 – 1)	0.70 ± 0.082 (0.6 – 0.8)	0.746
AUCpre/trapezius muscle AUC pre-treatment value	3.702 ± 1.500 (1.53 – 6.73)	4.070 ± 1.238 (3.16 – 5.89)	0.536
K(trans)pre/trapezius muscle K(trans) pre-treatment value	5.625 ± 2.964 (1.525 – 12.929)	4.735 ± 0.388 (4.280 – 5.230)	0.702
Post-treatment residual tissue maximum submucosal enhancement thickness (mm)	3.31 ± 4.135 (0 – 10)	22.75 ± 17.095 (7 – 45)	0.002
Post-treatment residual tissue median ADC value (x10^{-3} mm^2/s) [ADCpost]	1.545 ± 0.230 (0.961 – 1.963)	1.058 ± 0.267 (0.788 – 1.328)	0.002
Post-treatment residual tissue AUC value [AUCpost]	105.106 ± 51.140 (35.37 – 260.88)	123.625 ± 49.264 (59.77 – 162.90)	0.425
Post-treatment tumour K(trans) value (x 10^{-3} min) [K(trans)pre]	181.8 ± 201.8 (25,54 – 787.92)	142.42 ± 67.63 (56.24 – 215.45)	0.659
ADCpost/trapezius muscle ADC post-treatment value	1.246 ± 0.188 (0.8 –1.5)	0.875 ± 0.150 0.8 – 1.1)	0.002
AUCpost/trapezius muscle AUC post-treatment value	3.555 ± 1.244 (1.13 – 6.07)	4.347 ± 0.821 (3.52 – 5.43)	0.177
K(trans)post/trapezius muscle K(trans) post-treatment value	5.159 ± 4.570 (1.177 – 23.070)	4.864 ± 0.654 (4.087 – 5.412)	0.359
ADCpost-pre	0.705 ± 0.267 (0.16 – 1.20)	0.265 ± 0.409 (-0.13 – 0.70)	0.052
ADCpost-pre%	92.12 ± 44.101 (21 – 209)	20.75 ± 36.482 (-13 – 65)	0.005
AUCpost/pre	1.266 ± 0.795 (0.40 – 3.70)	1.245 ± 0.371 (1.01 – 1.80)	0.659
AUCpost/pre/trapezius muscle	1.085 ± 0.114 (0.37 – 2.70)	1.098 ± 0.575 (0.92 – 1.18)	0.791
K(trans)post/pre	1.067 ± 1.410 (0.06 – 5.66)	0.969 ± 0.633 (0.48 – 1.90)	0.498
K(trans)post/pre/trapezius muscle	1.076 ± 0.910 (0.307 – 4.012)	1.027 ± 0.115 (0.869 – 1.143)	0.271

Table 5. Mean values, standard deviation and range of the results of the study.
ADC: apparent diffusion coefficient; AUC: area under the curve; P-value: probability value.

Figures

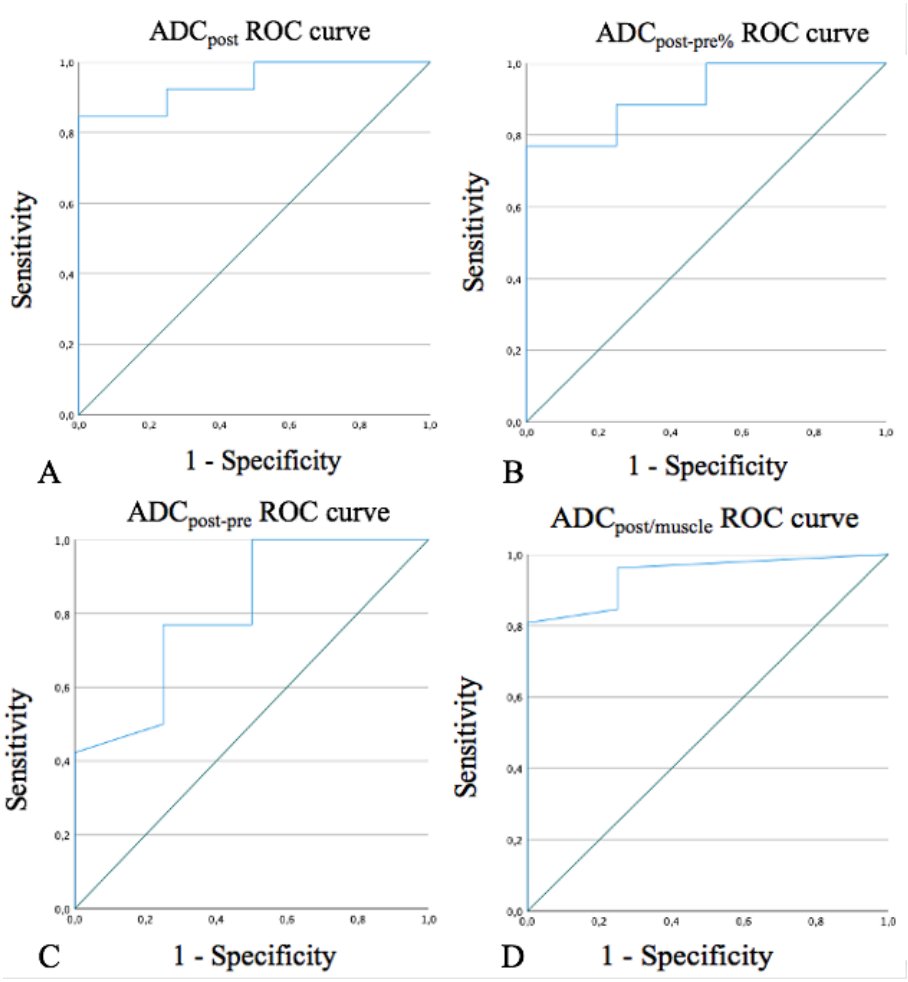

Figure 1. Receiver Operating Characteristic (ROC) curves for ADC_{post} values (a), $ADC_{post\text{-}pre\%}$ (b), $ADC_{post\text{-}pre}$ values (c), and $ADC_{post/muscle}$ values (d).

ADCpost: residual tissue mean ADC value.

ADCpost-pre%: residual tissue mean ADC value - tumour mean ADC value, expressed in % calculated as follow: $\frac{\text{ADCpost}-\text{pre x 100}}{\text{ADCpre}}$. Negative % indicates that ADCpost values are lower than ADCpre.

ADCpost-pre: residual tissue mean ADC value - tumour mean ADC value.

ADCpost/muscle: ratio between residual tissue ADC value and ipsilateral trapezius muscle ADC value measured on 3-4 month follow-up magnetic resonance imaging.

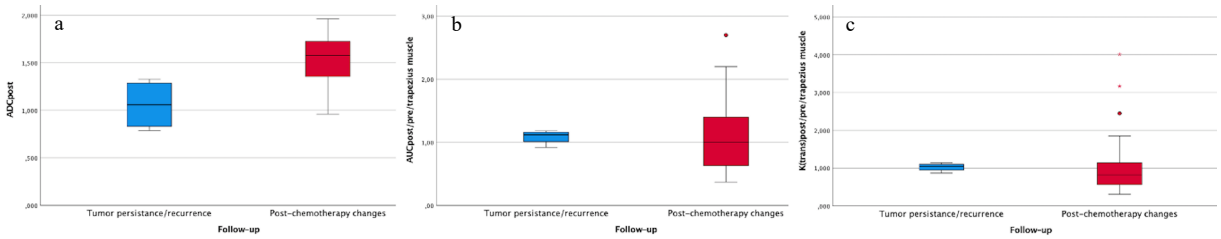

Figure 2. Box plot for post-treatment residual tissue AUC value (AUCpost, a), $\frac{\text{AUCpost}}{\text{AUC muscle post}} : \frac{\text{AUC pre}}{\text{AUC muscle pre}}$ (AUCpost/pre/trapezius muscle, b), and $\frac{\text{K(trans)post}}{\text{K(trans) muscle post}} : \frac{\text{K(trans) pre}}{\text{K(trans) muscle pre}}$ (K(trans)post/pre/trapezius muscle, c) in patients with tumour persistence/recurrences (blue box) and post-radiochemotherapy changes (red box).

AUC: area under the curve on dynamic contrast enhancement-perfusion weighted imaging.

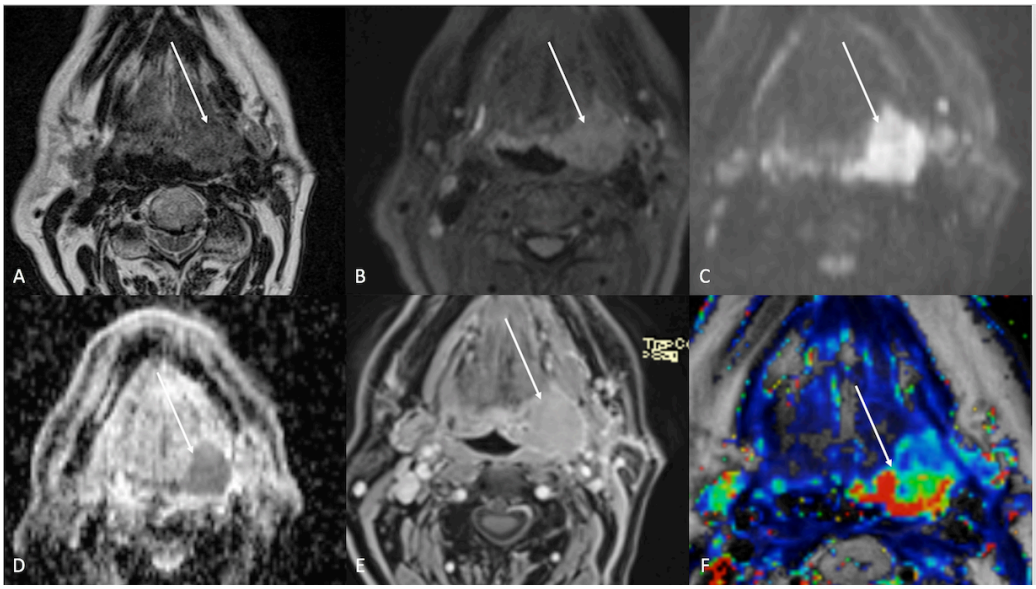

Figure 3. Pre-treatment Magnetic Resonance Imaging (MRI) of a 75-year-old male patient with Human Papilloma Virus positive carcinoma of the left palatine tonsil (T2N0; white arrows). MR images show a bulky tumour arising from the left palatine tonsil that extends into the ipsilateral amigdalo-glossus sulcus. The lesion shows hyperintense signal on T2-weighted (a), T2-weighet fat saturated (b), and diffusion weighted b_{800} images (c) compared to muscle signal, very low median apparent diffusion coefficient value (0.642 x 10^{-3} mm^2/s) (d), vivid and homogeneous enhancement on T1-weighted image after gadolinium contrast agent injection (e), and high K(trans) value (375,88 x 10^{-3} min) on dynamic contrast enhancement-perfusion weighted imaging (f).

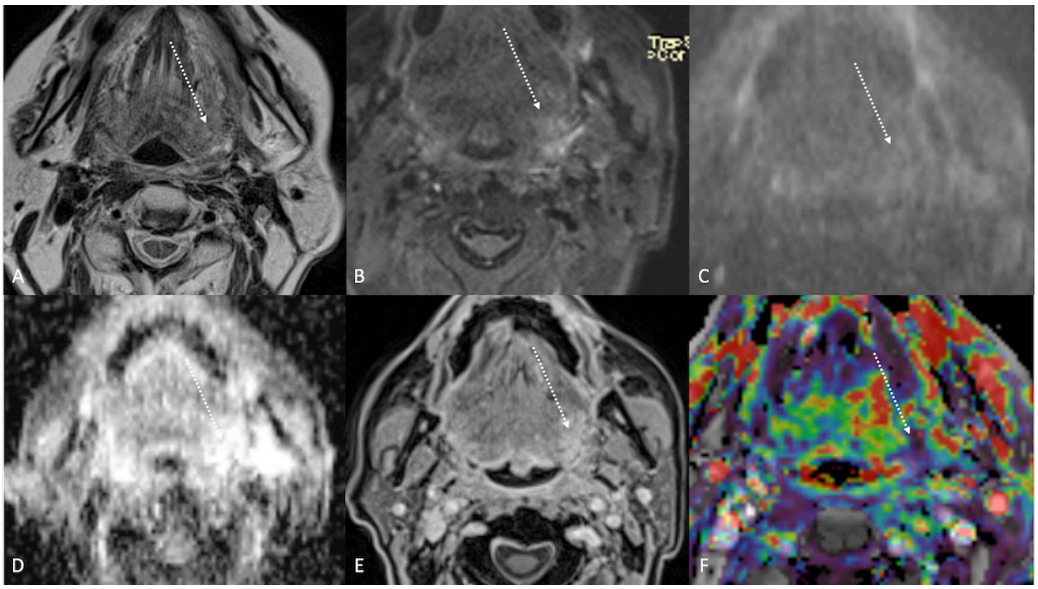

Figure 4. Same patient as Figure 3. Post-treatment Magnetic Resonance Imaging (MRI) shows post-radiochemotherapy (CRT) changes in a 75-year-old male patient treated for Human Papilloma Virus positive carcinoma of the left palatine tonsil (white stripped arrows). Post-CRT tissue shows slightly hyperintense signal on T2-weighted (a), and T2-weighted fat saturated (b) compared to signal muscle, hypointense signal on diffusion weighted b_{800} imaging (c), and median high apparent diffusion coefficient value (1.655 x 10^{-3} mm^2/s) (d). After gadolinium contrast agent injection, post-CRT tissue manifests ad an area of submucosal moderate enhancement (maximum tumour thickness: 10 mm) in the left amigdalo-glossus sulcus (e), and low K(trans) value (25,54 x 10^{-3} mm^2/s) on dynamic contrast enhancement-perfusion weighted imaging (f). Ratio between K(trans) values of the primitive tumour and of the residual tissue after CRT, standardized with respect to K(trans) value of the ipsilateral trapezius ($K(trans)_{post/pre/muscle}$), was 0.841.

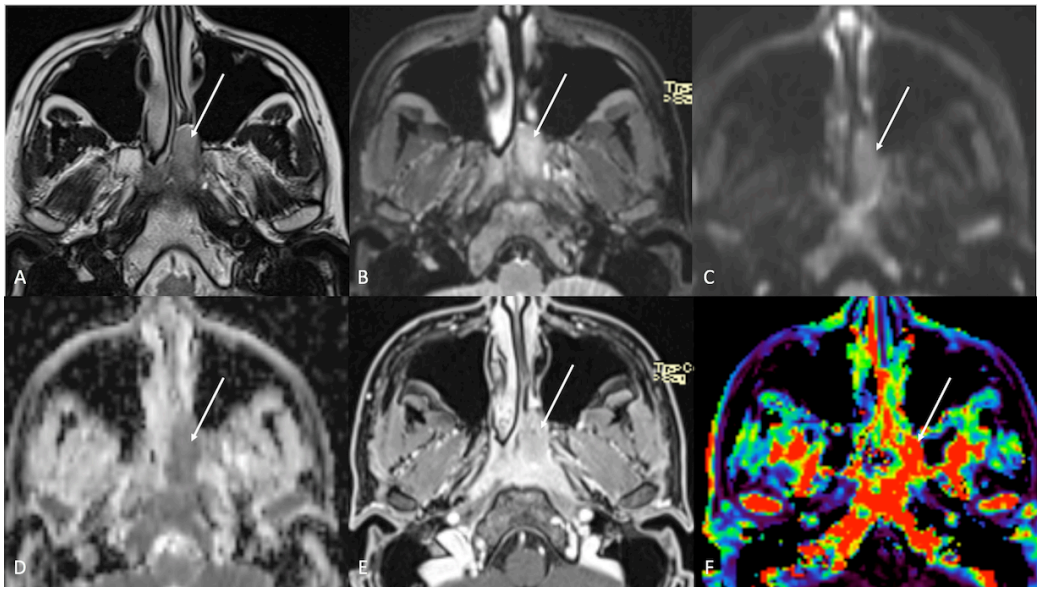

Figure 5. Pre-treatment Magnetic Resonance Imaging (MRI) of a 36-year-old female patient affected by nasopharyngeal carcinoma with tumoral extension to bilateral Ronsemüller fossa, left nasal choana, and middle skull base, and left lymph node metastasis (T3N3). MR images show a huge tumour arising from the left Ronsemüller fossa that invades the ipsilateral nasal choana (white arrows). The lesion shows hyperintense signal on T2-weighted (a), T2-weighet fat saturated (b), and diffusion weighted b_{800} images (c) compared to muscle signal, low median apparent diffusion coefficient value (0.732 x 10^{-3} mm^2/s) (d), vivid and homogeneous enhancement on T1-weighted image after gadolinium contrast agent injection (e), and intermediate K(trans) value (105,12 x 10^{-3} min) on dynamic contrast enhancement-perfusion weighted imaging (f).

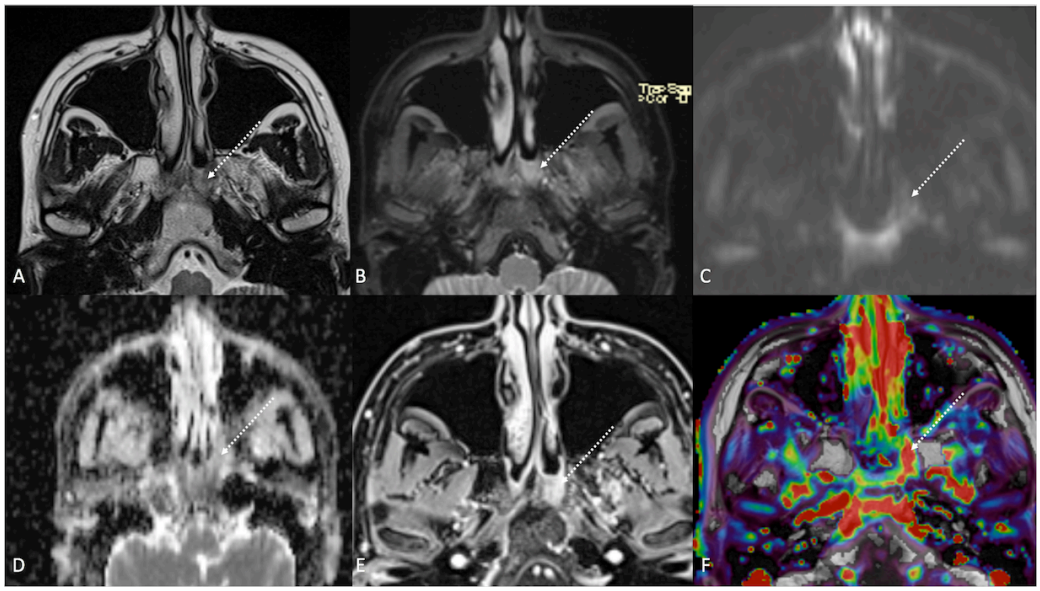

Figure 6. Same patient as Figure 5. Post-treatment Magnetic Resonance Imaging (MRI) shows post-radiochemotherapy (CRT) inflammatory changes in a 36-year-old female patient affected by nasopharyngeal carcinoma with tumoral extension to bilateral Ronsemüller fossa, left nasal choana, and middle skull base, and left lymph node metastasis (T3N3). Post CRT inflammatory tissue (withe stripped arrows) shows hyperintense signal on T2-weighted (a), T2-weighted fat saturated (b), and diffusion weighted b_{800} images due to «T2 shine-through» effect (c), and high median apparent diffusion coefficient value (1.534 x 10^{-3} mm^2/s) (d). After gadolinium contrast agent injection, post-CRT inflammatory tissue shows submucosal enhancement of 5 mm-thickness (e), and very high K(trans) value (595,25 x 10^{-3} mm^2/s) on dynamic contrast enhancement-perfusion weighted imaging (f). Ratio between K(trans) values of the primitive tumour and of the residual tissue after CRT, standardized with respect to K(trans) value of the ipsilateral trapezius ($K(trans)_{post/pre/muscle}$), was 3.171. These results suggest an increase in capillary permeability caused by CRT.

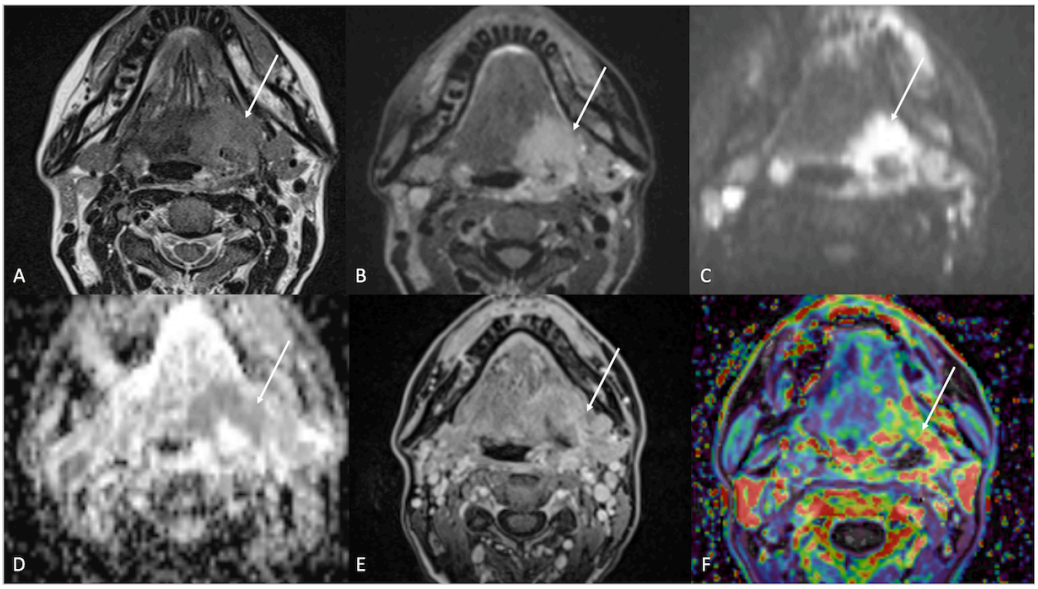

Figure 7. Pre-treatment Magnetic Resonance Imaging (MRI) of a 47-year-old female patient with Human Papilloma Virus negative carcinoma of the left palatine tonsil with buccal space and mandibular invasion, and ipsilateral lymph node metastasis (T4aN1). MR images show an infiltrative tumour arising from the left palatine tonsil that extends into the ipsilateral amigdalo-glossus sulcus, buccal fat space, and mandibular canal (white arrows). The lesion shows hyperintense signal on T2-weighted (a), T2-weighet fat saturated (b), and diffusion weighted b_{800} images (c) compared to muscle signal, low median apparent diffusion coefficient value (0.834 x 10^{-3} mm^2/s) (d), vivid and inhomogeneous enhancement on T1-weighted image after gadolinium contrast agent injection (e), and high K(trans) value (117,63 x 10^{-3} min) on dynamic contrast enhancement-perfusion weighted imaging (f).

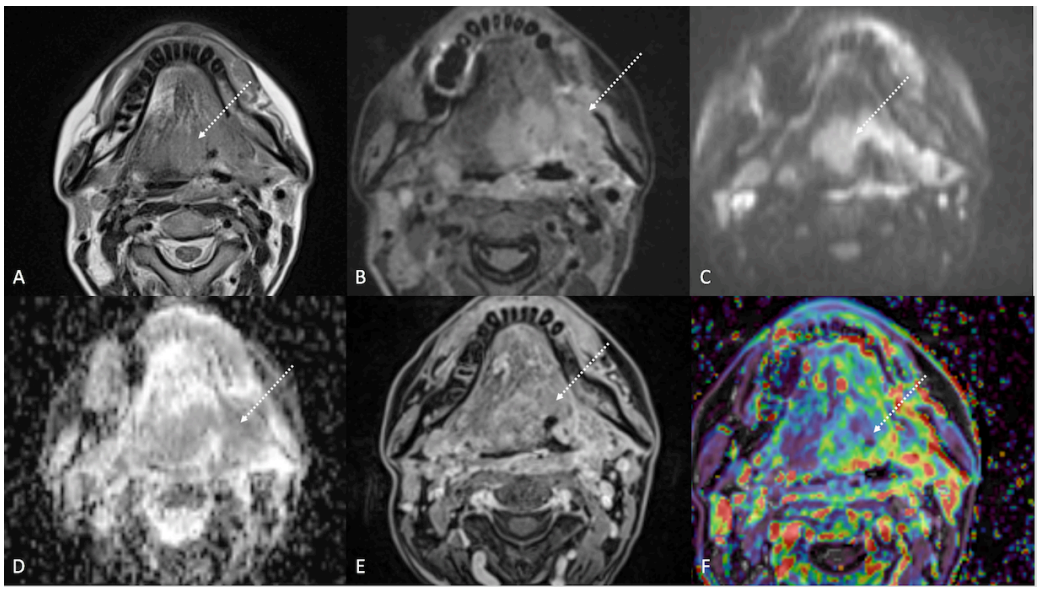

Figure 8. Same patient as Figure 7. Post-treatment Magnetic Resonance Imaging (MRI) shows tumour progression with wide extension to the extrinsic muscle of the contralateral tongue (maximum tumour thickness: 45 mm). Compared to pre-treatment MR, post-radiochemotherapy (CRT) residual tissue (withe stripped arrows) does not show significant changes in T2 signal (a, b), diffusion weighted b_{800} imaging (c), median apparent diffusion coefficient value (0.788 x 10^{-3} mm^2/s), and grade of enhancement after gadolinium contrast injection (e). K(trans) value of the tumour (56,24 x 10^{-3} min) decreased on dynamic contrast enhancement-perfusion weighted imaging (f), compared to pre-treatment MR. However, ratio between K(trans) values of the primitive tumour and of the residual tissue after CRT, standardized with respect to K(trans) value of the ipsilateral trapezius ($K(trans)_{post/pre/muscle}$), was 1.143. These results suggest little or no reduction in tumour neoangiogenesis after CRT.

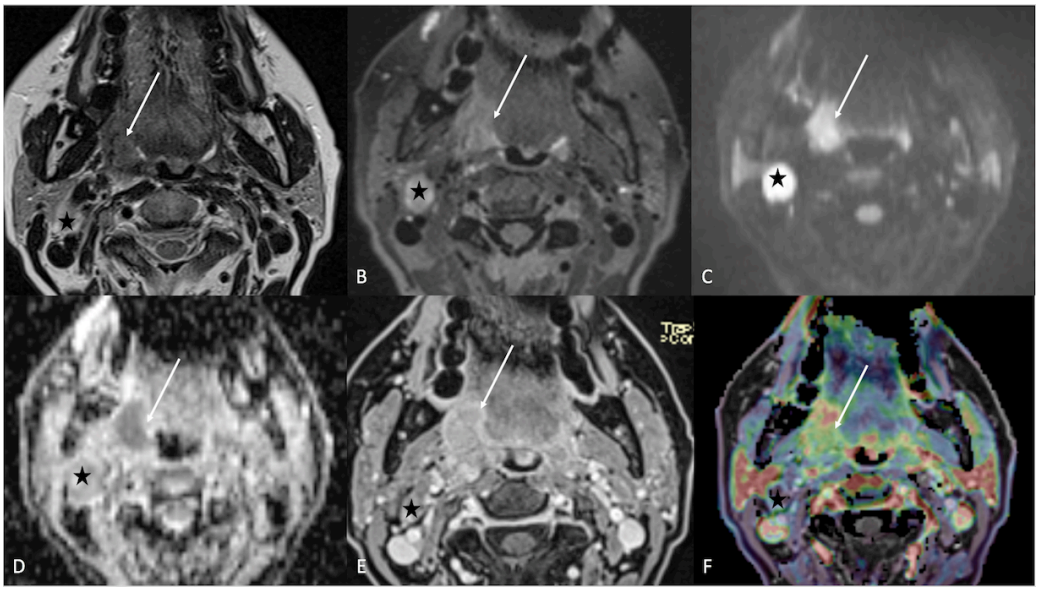

Figure 9. Pre-treatment Magnetic Resonance Imaging (MRI) of a 63-year-old female patient with Human Papilloma Virus positive carcinoma of the right palatine tonsil with ipsilateral lymph node metastasis (*) (T2N1). MR images show a T2 tumour arising from the right palatine tonsil that extends into the ipsilateral amigdalo-glossus sulcus. The lesion appears isointense on T2-weighted (a), hyperintense on T2-weighet fat saturated (b), and diffusion weighted b_{800} images (c) compared to muscle signal. It shows low median apparent diffusion coefficient value (0.724 x 10^{-3} mm^2/s) (d), moderate homogeneous enhancement on T1-weighted image after gadolinium contrast agent injection (e), and intermediate K(trans) value (92,84 x 10^{-3} min) on dynamic contrast enhancement-perfusion weighted imaging (f).

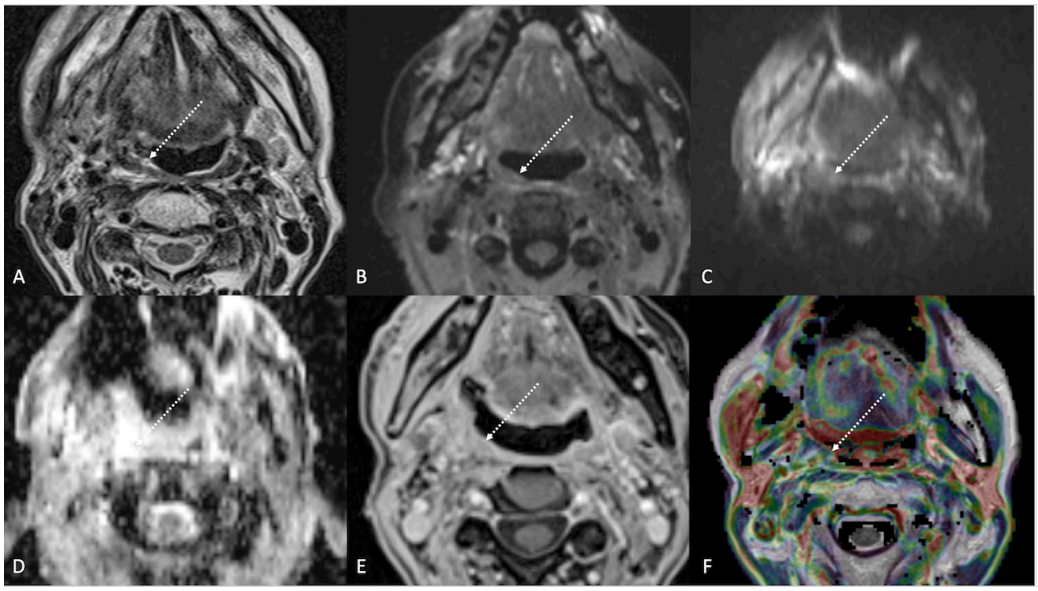

Figure 10. Same patient as Figure 9. Post-treatment Magnetic Resonance Imaging (MRI) shows post-radiochemotherapy (CRT) fibrotic changes in a 63-year-old female patient with Human Papilloma Virus positive carcinoma of the right palatine tonsil ipsilateral lymph node metastasis (T2N1). Post CRT fibrotic tissue (withe stripped arrows) shows hypointense signal on T2-weighted (a), T2-weighted fat saturated (b), and diffusion weighted b_{800} images (c), and intermediate median apparent diffusion coefficient value (1.442 x 10^{-3} mm^2/s) (d). After gadolinium contrast agent injection, post-CRT fibrotic tissue shows no submucosal enhancement (e), and low K(trans) value (48,36 x 10^{-3} mm^2/s) on dynamic contrast enhancement-perfusion weighted imaging (f).

Ratio between K(trans) values of the primitive tumour and of the residual tissue after CRT, standardized with respect to K(trans) value of the ipsilateral trapezius ($K(trans)_{post/pre/muscle}$), was 0.307. These findings are pathognomonic of post-CRT scar.